Monthly Notices
of the
ROYAL ASTRONOMICAL SOCIETY

MNRAS **435,** 1680–1700 (2013) doi:10.1093/mnras/stt1408
Advance Access publication 2013 September 4

SN Ia host galaxy properties from Sloan Digital Sky Survey-II spectroscopy

Jonas Johansson,[1,2]★ Daniel Thomas,[1,3] Janine Pforr,[1,4] Claudia Maraston,[1,3] Robert C. Nichol,[1,3] Mathew Smith,[5] Hubert Lampeitl,[1] Alessandra Beifiori,[1,6] Ravi R. Gupta[7] and Donald P. Schneider[8,9]

[1]*Institute of Cosmology and Gravitation, Dennis Sciama Building, Burnaby Road, Portsmouth PO1 3FX, UK*
[2]*Max-Planck-Institut für Astrophysik, Karl-Schwarzschild-Str. 1, D-85741 Garching, Germany*
[3]*SEPnet, South East Physics Network*
[4]*National Optical Astronomy Observatory, 950 N. Cherry Ave., Tucson, AZ 85719, USA*
[5]*Department of Physics, University of Western Cape, Bellville 7535, Cape Town, South Africa*
[6]*Max-Planck-Institut für Extraterrestrische Physik, Giessenbachstrasse, D-85748 Garching, Germany*
[7]*Department of Physics and Astronomy, University of Pennsylvania, 209 South 33rd Street, Philadelphia, PA 19104, USA*
[8]*Department of Astronomy and Astrophysics, The Pennsylvania State University, 525 Davey Laboratory, University Park, PA 16802, USA*
[9]*Institute for Gravitation and the Cosmos, The Pennsylvania State University, 525 Davey Laboratory, University Park, PA 16802, USA*

Accepted 2013 July 29. Received 2013 July 25; in original form 2012 November 2

ABSTRACT

We study the stellar populations of Type Ia supernova (SN Ia) host galaxies using Sloan Digital Sky Survey (SDSS)-II spectroscopy. The main focus is on the relationships of SN Ia properties with stellar velocity dispersion and the stellar population parameters age, metallicity and element abundance ratios. We concentrate on a sub-sample of 84 SNe Ia from the SDSS-II Supernova Survey and find that SALT2 stretch factor values show the strongest dependence on stellar population age. Hence, more luminous SNe Ia appear in younger stellar progenitor systems. No statistically significant trends in the Hubble residual with any of the stellar population parameters studied are found. Moreover, the method of photometric stellar mass derivation affects the Hubble residual–mass relationship. For an extended sample (247 objects), including SNe Ia with SDSS host galaxy photometry only, the Hubble residual–mass relationship behaves as a sloped step function. In the high-mass regime, probed by our host spectroscopy sample, this relationship is flat. Below a stellar mass of $\sim 2 \times 10^{10}\,\mathrm{M}_{\odot}$, i.e. close to the evolutionary transition mass of low-redshift galaxies, the trend changes dramatically such that lower mass galaxies possess lower luminosity SNe Ia after light-curve corrections. The sloped step function of the Hubble residual–mass relationship should be accounted for when using stellar mass as a further parameter for minimizing the Hubble residuals.

Key words: supernovae: general – galaxies: abundances – cosmological parameters – cosmology: observations – distance scale – large-scale structure of Universe.

1 INTRODUCTION

Type Ia supernovae (SNe Ia) are useful for constraining cosmological parameters. Their large peak luminosities can probe vast cosmological distances and connect redshift space to luminosity distance. This property led to the discovery of an accelerating expansion of the Universe (Riess et al. 1998; Perlmutter et al. 1999).

To be ideal cosmology indicators, all SN Ia explosions should have the same peak luminosity, but this is not the case. Observed SNe Ia span a range in peak luminosity accompanied by varying decline rates (Phillips 1993), i.e. the peak luminosity decreases with increasing decline rate. This variation can be corrected for to find a standardized peak luminosity. Several light-curve (LC) fitting tools are available (Guy et al. 2007; Jha, Riess & Kirshner 2007; Conley et al. 2008; Kessler et al. 2009a), where the shape of the LC and the colours are corrected to match a standardized peak luminosity. The LC shape correction is known as stretch factor.

Correcting the LC increases the precision of the derived luminosity distances and consequently reduces the scatter in the redshift–distance relation, thus increasing the precision of the derived cosmological parameters. However, even after LC corrections there is an intrinsic scatter of $\sim$0.12 mag (Lampeitl et al. 2010b; Campbell

★E-mail: jonasj@MPA-Garching.MPG.DE

et al. 2013). Understanding systematic uncertainties in the derived SN Ia LC parameters is therefore key to improving SN cosmology.

The accepted model for SNe Ia is thermonuclear explosion of a carbon–oxygen white dwarf (WD) that reaches the Chandrasekhar limit (Whelan & Iben 1973; Hillebrandt & Niemeyer 2000). Two different channels have been proposed, either the single-degenerate (SD) scenario where mass is accreted from an evolved main-sequence binary companion or the double-degenerate (DD) case of merging of two WDs (e.g. Woosley & Weaver 1986; Branch et al. 1995; Hoflich, Khokhlov & Wheeler 1995; Yungelson & Livio 2000; Branch 2001; Greggio 2005). This raises the possibility that different SN Ia populations may be present.

The delay time, i.e. the time between progenitor formation and explosion, in the DD scenario is determined by the lifetime of the WD progenitors and the orbit of the two binary stars. The delay time of an SD system partly depends upon the main-sequence lifetime of the companion star. A wide variety of delay times have been observationally suggested, ranging from <1 Gyr (Barris & Tonry 2006; Aubourg et al. 2008) to >2 Gyr (Gal-Yam & Maoz 2004; Strolger et al. 2004, 2005). Considering several different progenitor systems, theoretical models find the SN Ia rate (SNR) to peak at delay times below or close to 1 Gyr (Yungelson & Livio 2000; Greggio 2005; Ruiter et al. 2011). The SNR of most progenitor systems then smoothly declines and becomes 10–100 times lower at delay times of $\sim$10 Gyr. Comparing observed delay times to theoretical predictions can constrain possible progenitor systems.

It is well established that the SNR is higher in star-forming late-type than in passively evolving early-type galaxies (e.g. Oemler & Tinsley 1979; van den Bergh 1990; Mannucci et al. 2005; Sullivan et al. 2006; Smith et al. 2012). Moreover, several authors found a dependence on host galaxy mass for the decline rate of SNe Ia (Howell et al. 2009; Neill et al. 2009; Sullivan et al. 2010). Since galaxy mass correlates with stellar population parameters and properties of the interstellar medium (Tremonti et al. 2004; Gallazzi et al. 2005; Thomas et al. 2010), more fundamental correlations such as with stellar population age, metallicity and element abundance ratios may be expected. The tight relation between the SN Ia decline rate and peak brightness indicates a primary dependence of luminosity on one of these parameters, thus holding important information about the properties of SN Ia progenitor systems.

The luminosity of SNe Ia arises from the radioactive decay of ^{56}Ni to ^{56}Co, that then decays to ^{56}Fe (Colgate & McKee 1969; Arnett 1982), such that the peak brightness depends on the ^{56}Ni mass. It has been suggested that metallicity is a second parameter controlling the SN Ia LC (Podsiadlowski et al. 2008; Kasen, Röpke & Woosley 2009), where Timmes, Brown & Truran (2003) show theoretically that metallicity effects, in the range 1/3–3 $Z_{\odot}$, can induce a 25 per cent variation in the ^{56}Ni mass. Theoretical models have also predicted that the carbon mass fraction, determined by the metallicity and mass of the WD progenitor, is responsible for SN Ia luminosity variations (Umeda et al. 1999). Dependences of SN Ia properties on element ratios, such as C/Fe, may thus be expected. The ratio of light elements to Fe is also interesting because Fe dominates the LC of SNe Ia and could well influence some of the SN Ia properties.

Observationally, it has been found that SNe Ia in star-forming galaxies show slower decline rates as compared to SNe Ia in passively evolving galaxies (Sullivan et al. 2006; Howell et al. 2009; Neill et al. 2009; Lampeitl et al. 2010b; Smith et al. 2012). On the other hand, Gallagher et al. (2005) did not find any decline rate dependence on the star formation rate (SFR) in star-forming galaxies. Cooper, Newman & Yan (2009) showed that the SNR of blue, star-forming galaxies is higher in regions of lower galaxy density and suggested that this dependence is driven by gas-phase metallicity effects. Moreover, several authors have recently found dependences on stellar population age and/or stellar/gas-phase metallicity for the SN Ia decline rate (Hamuy et al. 2000; Gallagher et al. 2005; Howell et al. 2009; Neill et al. 2009; Gupta et al. 2011). However, in most cases either fairly small samples have been used ($<$30 objects; Hamuy et al. 2000) or metallicity has been measured indirectly (Cooper et al. 2009; Howell et al. 2009; Neill et al. 2009). It is therefore desired to study the full range of stellar population parameters for a statistically significant sample of SN Ia host galaxies, which was the main aim of this study.

Correlations between the SN Ia peak luminosity and stellar population parameters should ideally be eliminated through LC fitting, due to the tight correlation between the peak luminosity and decline rate. However, if such correlations remain even after LC corrections, the previously mentioned non-negligible scatter in the redshift–distance relation could be reduced. These relationships are important to identify, especially for wide redshift surveys, as the stellar population parameters age and metallicity change over cosmic time. Since the scatter in the redshift–distance relation is small, high-quality data are required to detect dependences on host galaxies. To date galaxy mass and metallicity have shown to be the best candidates for such dependences (Gallagher et al. 2008; Howell et al. 2009; Neill et al. 2009; Kelly et al. 2010; Lampeitl et al. 2010b; Sullivan et al. 2010; D'Andrea et al. 2011; Gupta et al. 2011). This led to the introduction of stellar mass as a further parameter, besides LC stretch factor and colour, to minimize the scatter in the redshift–distance relation (e.g. Lampeitl et al. 2010b; Sullivan et al. 2010). However, it is desirable to find the fundamental parameter of this scatter and, again, to do this the full range of stellar population parameters is needed for a statistically significant sample.

In this paper, we study host galaxies of SNe Ia from the Sloan Digital Sky Survey (SDSS; York et al. 2000)-II Supernova Survey (Frieman et al. 2008) for which SDSS-II spectroscopy is available. This allows us to investigate SN Ia host galaxy stellar populations through Lick absorption line indices (e.g. Worthey et al. 1994; Trager et al. 1998). These are defined for 25 prominent absorption features in the optical and are useful for breaking the age–metallicity degeneracy, deriving element ratios, and they are insensitive to dust reddening (MacArthur 2005). Gallagher et al. (2008) is to date the only study in the literature that relies on Lick indices for studying SN Ia host galaxies, based on a sample of 29 early-type galaxies [Hamuy et al. (2000) study a sample of five SN Ia host galaxies through Lick indices]. The SDSS-II Supernova Survey in combination with SDSS-II spectroscopy allows us to significantly improve upon this sample size. We use the method presented in Johansson, Thomas & Maraston (2012), which is based on up-to-date stellar population models of absorption line indices from Thomas, Maraston & Johansson (2011, hereafter TMJ), to derive age and metallicity together with a range of element abundance ratios including C/Fe as well as O/Fe, Mg/Fe, N/Fe, Ca/Fe and Ti/Fe. This allows us to explore the full range of stellar population parameters to search for the fundamental parameter of the variations of SN Ia properties.

In addition, we determine stellar masses from SDSS-II photometry using different methodologies of photometric spectral energy distribution (SED) fitting to study systematic uncertainties in the proposed dependence of the scatter in the redshift–distance relation on stellar mass.

The paper is organized as follows. The data sample used is described in Section 2 along with the description of our derivation of

spectroscopic stellar population parameters and stellar masses. The relationships between SN Ia properties and host galaxy parameters are presented in Section 3. We discuss the results in Section 4 and concluding remarks are given in Section 5.

2 DATA SAMPLE

The sample used in this study is drawn from the SDSS-II Supernova Survey (Frieman et al. 2008). The SDSS 2.5 m telescope (York et al. 2000; Gunn et al. 2006), located at the Apache Point Observatory, is equipped with a multi-object spectrograph (Smee et al. 2012) and wide-field CCD camera (Gunn et al. 1998). During the 8 yr period of 2000–2008, the SDSS-I and SDSS-II surveys obtained deep images in the SDSS *ugriz* filters (Fukugita et al. 1996) and spectroscopy for more than 930 000 galaxies.

The SDSS-II SN survey was performed over a 3 yr period (2005–2007) to repeatedly image transient objects in the SDSS 'Stripe 82' region. Thousands of potential SN candidates were observed. Out of these, 890 were identified as SN Ia candidates including 551 with spectroscopic confirmation (Holtzman et al. 2008; Sako et al. 2008; Sako et al., in preparation). The SDSS-II SN sample has been used for cosmological analyses (Kessler et al. 2009b; Sollerman et al. 2009; Lampeitl et al. 2010a) as well as photometric and spectroscopic studies of SN Ia host galaxy properties (Lampeitl et al. 2010b; D'Andrea et al. 2011; Gupta et al. 2011; Smith et al. 2012).

Following Lampeitl et al. (2010b), we include photometrically classified SNe Ia, to ensure a more complete sample. Based on the Bayesian LC fitting of Sako et al. (2008), these SNe have an LC consistent with being a Type Ia. The contamination of non-SN Ia objects using the photometric classification scheme is only ∼3 per cent (Dilday et al. 2010).

In this work, we focus on a sub-sample of SNe Ia with available SDSS-II host galaxy spectroscopy (from now on referred to as the host spectroscopy sample). The SN Ia coordinates and redshifts have been cross-matched with the corresponding parameters in the SDSS-II Data Release 7 (DR7) catalogue (Abazajian et al. 2009) to identify the nearest object with a spectrum within a 0.″25 radius, resulting in a host spectroscopy sample of 292 objects. A similar cross-match has been made to acquire co-add photometry from the SDSS 'Stripe 82' region (Annis et al. 2011). The host galaxy coordinates from both runs have been further cross-matched to ensure that the spectroscopy and photometry belong to the same object. Out of the 292 SNe in the host spectroscopy sample, 138 (47 per cent) are spectroscopically confirmed SNe Ia. For redshifts below 0.21, the fraction of spectroscopically confirmed SNe Ia increases to 60 per cent. This is also the redshift range covered by the final sample selection (see Section 2.3) used in the main analysis.

In addition to the host spectroscopy sample, we include in Section 3.4.2 SN Ia host galaxies with available SDSS photometry only, to extend the stellar mass analysis. This extended photometric sample adds another 102 objects from the study of Lampeitl et al. (2010b) and is described in detail in Section 3.4.2.

The derived SN Ia properties, host galaxy parameters and final selection of the host spectroscopy sample are described in the following sections.

2.1 SN Ia properties

The LC fitting technique follows Lampeitl et al. (2010b) to which the reader is referred for more details. A summary of the main features is presented here.

A number of LC fitting methods exist in the literature and several authors have confirmed that scaling relations between SN Ia and host galaxy parameters are robust against different analysis algorithms (Kelly et al. 2010; Lampeitl et al. 2010b; Sullivan et al. 2010). For this work, the distance modulus to an SN Ia is determined using the SALT2 (Guy et al. 2007) LC fitting method and is defined as

$$\mu = m_B - M + \alpha x_1 - \beta c + \mu_{\rm corr}(z), \quad (1)$$

where $m_B = 10.635 - 2.5\log(x_0)$. x_0, x_1 and c are SN parameters determined through fitting of the individual LC, and correspond to the peak magnitude, stretch and colour of each SN. We also include a correction for Malmquist bias ($\mu_{\rm corr}(z)$) which is discussed in Campbell et al. (2013). In equation (1), M is the absolute peak magnitude of a standard SN Ia (assumed to be −19.2 for this analysis), and α and β are global SALT2 parameters that describe the relationship between the stretch and colour of an SN Ia and the absolute brightness.

These parameters are determined by minimizing the scatter in the distance–redshift relation or the Hubble residual (HR)

$$\mathrm{HR} = \mu_{\rm SN}(M_B, \alpha, \beta) - \mu_{\rm cosmo}(z, H_0, \Omega_{\rm m}, \Omega_\Lambda), \quad (2)$$

where H_0 is the Hubble constant, $\Omega_{\rm m}$ is the density parameter for matter and Ω_Λ is the density parameter for the cosmological constant. We aim at detecting systematic trends in the derived HR and adopt $H_0 = 73.8$ km s^{-1} Mpc^{-1} (Riess et al. 2011), $\Omega_{\rm m} = 0.27$ and $\Omega_\Lambda = 0.73$ to match the best-fitting cosmology for our sample. Several different sample selections are used in this work and the HR are derived for each individually, with corresponding α and β values presented in the relevant sections.

For a negative HR, i.e. $\mu_{\rm cosmo} > \mu_{\rm SN}$, the cosmology places the SNe Ia at a greater distance than the peak luminosity predicts. Hence, after correcting for LC shape and colour, a negative HR indicates an SN Ia that is brighter than the fiducial average peak luminosity.

2.2 Host galaxy properties

The aim of this work is to analyse the host galaxy properties of SNe Ia from a spectroscopic point of view, particularly using absorption line indices. For this purpose, we need clean galaxy absorption spectra, free from contaminating emission lines. Absorption line indices are measured on the clean spectra and analysed using single stellar population models. We use the method detailed in Thomas et al. (2010) and Johansson et al. (2012) of which we provide a brief summary in the following section.

2.2.1 Kinematics and Lick indices

We utilize the fitting code GANDALF (Sarzi et al. 2006), which is based on the penalized pixel-fitting (PPXF) method of Cappellari & Emsellem (2004), to obtain clean absorption spectra. A brief description of the code is given here, while the reader is referred to Sarzi et al. (2006) and Cappellari & Emsellem (2004) for details. GANDALF/PPXF simultaneously fits stellar templates and emission-line Gaussians to galaxy spectra. The result is a separation of emission and absorption spectra. As stellar templates we adopt the single stellar population SEDs of Maraston & Strömbäck (2011). These have a fixed spectral resolution of 2.54 Å (Beifiori et al. 2011), i.e. close to the SDSS resolution of $R \sim 2000$. Besides the clean absorption spectra, other useful outputs of GANDALF/PPXF are stellar and gas kinematics, $E(B-V)$ dust reddening and emission-line fluxes/equivalent widths (EWs).

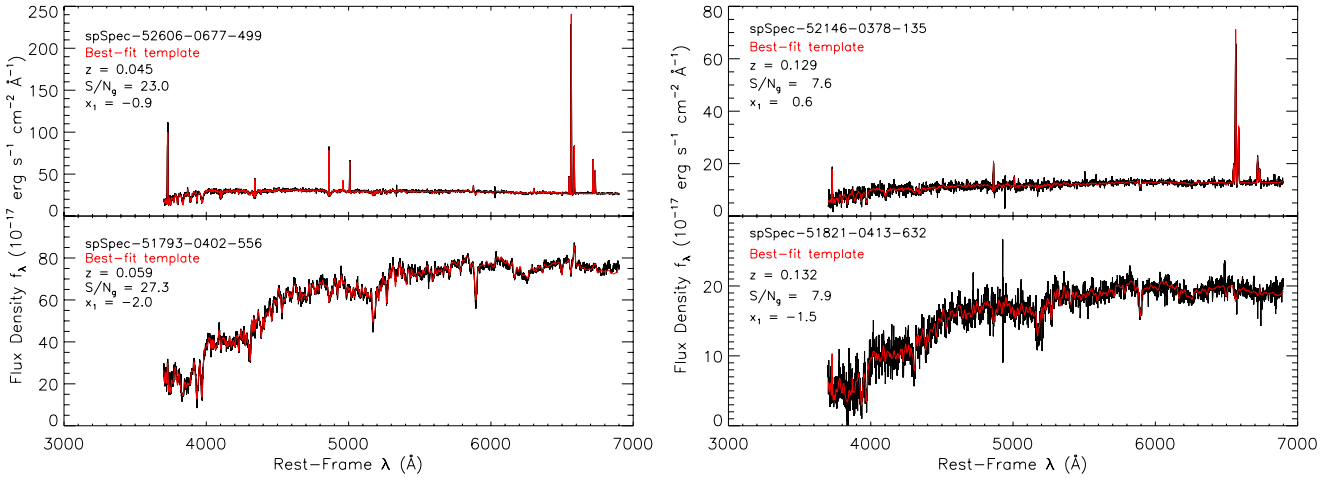

Figure 1. Four examples of host galaxy spectra (black SEDs) at rest-frame wavelength and with the best-fitting model templates from GANDALF/PPXF (red SEDs) overlaid. The top and lower panels show galaxies hosting SNe Ia with large and small stretch factor values, respectively, as given by the labels. The left- and right-hand panels show high- and low-S/N spectra, with values given by the labels. The redshift for each object is also indicated by the labels.

Fig. 1 shows four examples of host galaxy spectra (black SEDs) with varying stretch factor values (x_1) and signal-to-noise ratios (S/N) per pixel (∼1 Å at 4500 Å) in the g band of the spectra, as given by the labels. The corresponding best-fitting stellar templates from GANDALF/PPXF (red SEDs) are also shown. Prominent emission lines are visible in the galaxies hosting high stretch factor values.

The Lick system consists of definitions of absorption line indices for 25 prominent absorption features in the optical (Worthey et al. 1994; Trager et al. 1998). We measure the Lick indices on the clean absorption spectra, free from contaminating emission lines, using the latest definitions of Trager et al. (1998). The resolution of the spectra is downgraded to the Lick/IDS resolution (that of the models, ∼8–10 Å; Worthey & Ottaviani 1997) prior to measuring the indices. The index measurements are then corrected for velocity dispersion broadening, using the velocity dispersions found by GANDALF/PPXF together with the best-fitting stellar templates. The Lick indices are measured on the best-fitting stellar templates broadened to the Lick/IDS resolution, both before and after further broadening with respect to the velocity dispersion measurements. The difference between these two measurements gives the correction factor which we apply to the Lick indices measured on the galaxy spectra. Using the error vectors provided with each SDSS spectrum, we estimate Lick index errors through Monte Carlo simulations.

It is important to note that these are all standard procedures. Hence, our derived Lick indices can be compared directly to other galaxy samples in the literature. This holds for samples with flux-calibrated spectra, as the Lick indices are sensitive to the instrumental configuration. When comparing Lick indices from different samples based on non-flux-calibrated spectra, the common procedure is to use standard stars observed with both instrumental configurations to determine possible offsets/calibrations in the Lick indices (e.g. Johansson, Thomas & Maraston 2010). In this work, we fit the TMJ models to the observed Lick indices. The TMJ models are updated versions of the Thomas et al. (2003) models and are based on the flux-calibrated Medium-resolution Isaac Newton Telescope library of empirical spectra (MILES; Sánchez-Blázquez et al. 2006; Johansson et al. 2010). Hence, the models are no longer tied to the non-flux-calibrated Lick/IDS system, making standard star-derived offsets unnecessary when using flux-calibrated galaxy spectra. Lick index offsets are crucial when adopting stellar population models based upon non-flux-calibrated stellar libraries, such as the Lick/IDS library (e.g. Worthey et al. 1994), due to the sensitivity to the instrumental configuration of the Lick indices as mentioned above.

2.2.2 *Stellar population parameters*

From the derived Lick indices, we compute light-weighted stellar population parameters that are very sensitive to recent star formation (Serra & Trager 2007; Thomas et al. 2010). The young stellar populations get more weight because they are brighter. The rate of SN Ia increases with decreasing stellar population age, e.g. it is ∼100 times higher in a young population compared to a 10 Gyr old population (e.g. Maoz, Mannucci & Brandt 2012). Hence, in a composite population with only a small fraction of young stars, it is still likely that an observed SN Ia originates from the young population and not from the old bulk population. Thus, using light-weighted parameters is the better choice when studying relations between SN Ia parameters and host stellar population parameters.

The derived stellar population parameters are age, total metallicity and the element abundance ratios accessible through integrated light spectroscopy of galaxies (O/Fe, Mg/Fe, C/Fe, N/Fe, Ca/Fe and Ti/Fe), using the iterative method described in detail in Johansson et al. (2012). This method is based on the TMJ stellar population models of absorption line indices. These are single stellar population models with variable element abundance ratios for the 25 Lick indices (Korn et al. 2005). Since several indices respond to variations of the same element abundances, we have developed an iterative method. A χ^2-minimization routine is used at each step to find the best-fitting model.

First, we determine the traditional light-averaged stellar population parameters age, total metallicity and α/Fe ratio from indices sensitive to these three parameters only. In the subsequent steps, we add in turn particular sets of indices that are sensitive to the element the abundance of which we want to determine. In each step, we re-run the χ^2-fitting code with a new set of models to derive the abundance of this element. This new set of models is a perturbation to the solution found for the base set and is constructed by keeping the stellar population parameters age, metallicity and α/Fe fixed while modifying the abundance of the element under consideration. The derivations of element abundances are iterated until the values

do not further change. At the end of the sequence, we re-determine the overall χ^2 using all indices together and re-derive the base parameters age, metallicity and α/Fe for the new set of element ratios. The whole procedure is iterated until the final χ^2 stops improving by more than 1 per cent.

An enhanced α/Fe ratio is characterized by a depression in Fe and reflects the ratio between total metallicity and iron abundance. Since O dominates the mass budget of total metallicity, the α/Fe parameter derived through our procedure can be reasonably interpreted as O/Fe. In Johansson et al. (2012), we therefore re-named the parameter α/Fe to O/Fe under the assumption that this ratio provides an indirect measurement of oxygen abundance, i.e.

$$[\mathrm{O/Fe}] \equiv [\alpha/\mathrm{Fe}]. \quad (3)$$

2.2.3 Stellar mass

We derive stellar masses (M_*) from photometry according to standard SED fitting as in Daddi et al. (2005) and Maraston et al. (2006) via the normalization of the SED. The SED fitting is performed using the HYPERZ code of Bolzonella, Miralles & Pelló (2000) with SDSS spectroscopic redshifts and Milky Way extinction-corrected *ugriz* magnitudes as input. Masses are derived using different sets of stellar population models, i.e. from Maraston (2005, hereafter M05) and Bruzual & Charlot (2003, hereafter). As is well known, the main difference between these models is the different treatment of the thermally pulsing asymptotic giant branch (TP-AGB) contribution in the M05 models. The TP-AGB affects the luminosity at near-IR wavelengths, but starts to be important at ∼6000 Å, in galaxies with stellar population ages between ∼0.2 and 2 Gyr (M05). Another difference is the earlier onset of the red giant branch (RGB) in the M05 models (∼0.5 Gyr) with respect to the BC03 models (∼1 Gyr; Ferraro et al. 2004; M05). This makes the M05 models redder at an earlier age with respect to the BC03 models, affecting the derivation of stellar mass (Maraston et al. 2006).

To obtain as robust total M_* as possible, we exclude internal reddening in the fitting procedure, following Pforr, Maraston & Tonini (2012). These authors find that the inclusion of galaxy internal reddening as a fit parameter generates masses that are often underestimated with respect to the true stellar mass. This result occurs because dust reddening combined with young model ages produces young dusty solutions as best fit, with low mass-to-light ratios (the age–dust degeneracy; see Renzini 2006). Furthermore, we exclude single burst templates which sometimes further increase the risk of getting underestimated stellar masses.

To compare with literature values, which usually include reddening, we further calculate stellar masses for the following options: M05 models with reddening ($\mathrm{M05_{red}}$), BC03 models without reddening and BC03 model with reddening ($\mathrm{BC03_{red}}$).

Throughout this paper, we also compare our derived stellar masses to those derived following Lampeitl et al. (2010b, hereafter L10). They derive masses through photometric SED fitting using the PÉGASE models (Fioc & Rocca-Volmerange 1997, 1999) and including reddening in the fitting procedure. The PÉGASE SEDs show a similarity to those of the BC03 models (see M05). From now on, we refer to these masses as the L10 masses.

2.2.4 Gas-phase metallicity

Gas-phase metallicities are derived from the EWs of the emission lines measured by GANDALF/PPXF (see Section 2.2.1). Several calibrations for the relationship between metallicity and emission-line ratios are available in the literature. Relative metallicities generally agree between the various calibrations, while absolute metallicities frequently disagree. The calibration of Kewley & Dopita (2002, hereafter KD02) is commonly used in the literature, but it is based on the [N II λ6583]/[O II λ3727] ratio. The large difference in wavelength between the [N II λ6583] and [O II λ3727] lines makes this ratio sensitive to dust reddening. Instead, we use the O3N2 index ($\log(([\mathrm{O\,III}]\lambda5007]/\mathrm{H}\beta)/([\mathrm{N\,II}]\lambda6583]/\mathrm{H}\alpha))$ which is not sensitive to dust reddening due to the proximity of the emission lines in both the [O III λ5007]/Hβ and [N II λ6583]/Hα ratios. The O3N2 index was calibrated with $12 + \log[\mathrm{O/H}]$ in Pettini & Pagel (2004, hereafter PP04):

$$(12 + \log[\mathrm{O/H}])_{\mathrm{PP04}} = 8.73 - 0.32 \times \mathrm{O3N2}; \quad (4)$$

Kewley & Ellison (2008) re-calibrated the metallicity from PP04 on to the KD02 metallicity and found the relationship

$$\begin{aligned}(12 + \log[\mathrm{O/H}])_{\mathrm{KD02}} = {} & 159.0567 \\ & - 54.185\,11 \times (12 + \log[\mathrm{O/H}])_{\mathrm{PP04}} \\ & + 6.395\,364 \times (12 + \log[\mathrm{O/H}])^2_{\mathrm{PP04}} \\ & - 0.247\,1693 \times (12 + \log[\mathrm{O/H}])^3_{\mathrm{PP04}}. \quad (5)\end{aligned}$$

Using equations (4) and (5) we determine metallicities for objects with detected emission lines. The presence of an active galactic nucleus (AGN) may strongly affect the derived metallicities since a stellar ionizing radiation field is assumed in the commonly used metallicity calibrations (Kewley & Ellison 2008). Hence, we will therefore not consider gas metallicities for purely classified AGN hosts, while transition objects between star formation and AGN are treated with caution. AGN classification is discussed later in Section 3.1.

2.3 Sample cuts

The numbers of SNe for the host spectroscopy sample are given in Table 1, where 'Spec. confirm' gives just the spectroscopically confirmed SNe Ia, for the different selection cuts described in this section.

The individual objects of the host spectroscopy sample are presented in Table 2 (the full version of this table is electronically available), where we provide SDSS-II Supernova Survey identification numbers, the SN classification technique used (Sp = spectroscopically, Ph = photometrically) and host galaxy coordinates and redshifts. We also provide sample cut designation, where f = final host spectroscopy sample selected through the cuts presented below.

Table 1. Numbers of the host spectroscopy sample before and after the different cuts. The second column gives the number of spectroscopically confirmed SNe Ia, and the third column gives both spectroscopically and photometrically identified SNe Ia.

Selection	Spec. confirm	Total[a]
Full	138	292
LC fitter cuts	116	196
Separation cut	105	183
Host spec. quality cuts	63	84

[a]Total number used in the main analysis including both spectroscopically and photometrically identified SNe Ia.

Table 2. Specifications for the host spectroscopy sample.

ID	Class.[a]	RA (°)	Dec. (°)	z	Sample[b]
691	Ph	329.7300	−0.4990	0.1310	m
701	Ph	334.6050	0.7976	0.2060	f
717	Ph	353.6280	0.7659	0.1310	
722	Sp	0.7060	0.7519	0.0870	f
739	Sp	14.5960	0.6794	0.1080	f
762	Sp	15.5360	−0.8797	0.1920	m
774	Sp	25.4640	−0.8767	0.0940	f

[a]SN classification: Sp = spectroscopic, Ph = photometric (see Section 2).
[b]Sample selection, f = final host spectroscopy sample (see Section 2.3), m = Master sample (see Section 3.4.2).
(This table is available in its entirety in a machine-readable form in the online journal. A portion is shown here for guidance regarding its form and content.)

2.3.1 *SN Ia cuts*

To avoid contamination by low-quality data, we cut the sample to exclude the lowest quality SN Ia observations. The accepted χ^2 of the LC fit probability from SALT2 is constrained and we remove everything with a reduced $\chi^2 > 3$ (L10). This cut removes 15 of the 292 candidates (5 per cent) and is useful for reducing the contamination of non-Ia SNe (see below for more details). Following L10, we retain SNe Ia with SALT2 parameters inside the ranges $-4.5 < x_1 < 2.0$ and $-0.3 < c < 0.6$, and remove anything with particularly large x_1/c uncertainties ($\Delta x_1 > 1.0$ and $\Delta c > 0.1$, after all other cuts these cuts discard two objects only). Outside these ranges, L10 found the derived parameters to be unreliable. These cuts of the fitted LC parameters reduce the total sample to 196 objects ('LC fitter cuts' in Table 1).

The sub-sample of photometrically confirmed SNe Ia contains contamination from non-Ia SNe, while the spectroscopic sample is free from such contamination. It is therefore not surprising that the LC fitter cuts remove a greater proportion of the total sample (∼33 per cent) compared to the spectroscopically confirmed sample (∼16 per cent), as the LC fitter cuts reduce the contamination of non-Ia SNe in photometrically confirmed samples of SNe Ia (Campbell et al. 2013).

It is possible that parameter gradients and local deviations from the integrated parameters will affect the results. Hence, we discard SNe Ia that are separated by more than 0.15 arcmin from the host galaxy, which is three times the SDSS fibre diameter (0.05 arcmin). This cut produces a sample of 183 objects.

2.3.2 *Host spectroscopy cuts*

Fig. 2 shows the errors, represented by contours, in the stellar population parameters age (upper panel), total metallicity (middle panel) and [O/Fe] (lower panel) as a function of the median S/N per pixel (∼1 Å at 4500 Å) in the g band. This is the same format as fig. 4 from Johansson et al. (2012); the errors are for 3802 SDSS early-type galaxies of the sample of Morphologically Selected Ellipticals in SDSS (MOSES; Schawinski et al. 2007; Thomas et al. 2010), derived using the same method based on absorption line indices adopted in this work (see Section 2.2). The orange lines connect median errors in bins of g-band S/N, while the green dashed lines show the linear behaviours below S/N = 30. The errors on stellar population parameters increase almost linearly with decreasing S/N

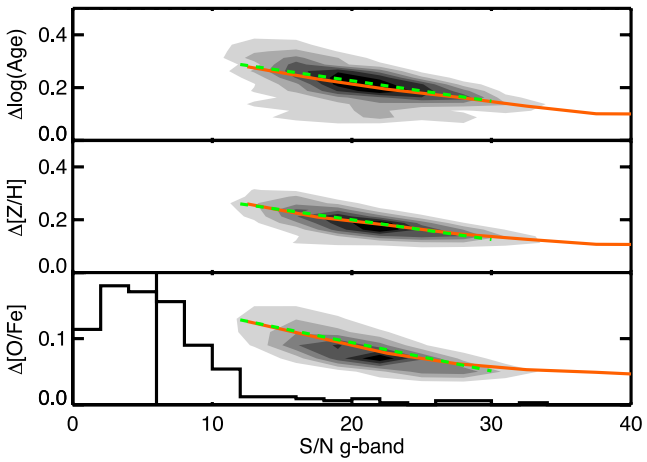

Figure 2. The relationship between the error in stellar population parameters and quality of galaxy spectra, in terms of S/N per pixel (∼1 Å at 4500 Å) in the g band (remake of fig. 4 from Johansson et al. 2012). Contours represent 3802 SDSS early-type galaxies from the MOSES sample (Thomas et al. 2010) for error in age (upper panel), total metallicity (middle panel) and [O/Fe] (lower panel). The orange lines connect the mean errors in bins of g-band S/N, while the green dashed lines show the linear behaviours below S/N = 30. The distribution of the full sample of SN Ia host galaxies (292 objects) is presented by the histogram, scaled by multiplying the binned histogram values with 0.18/60. The black vertical line represents the cut at S/N = 6, which defines our final sample.

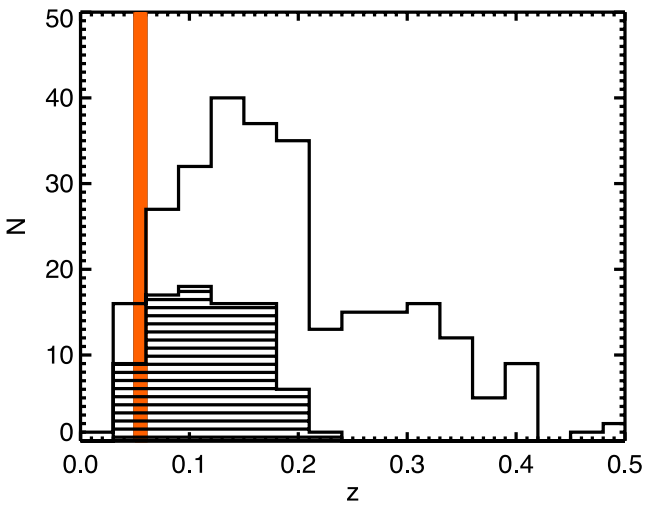

Figure 3. Distribution in redshift for the full sample of 292 SNe Ia (open histogram) and the final sample of 84 SNe Ia (dash-filled histogram). The orange area represents the redshift range covered by the early-type galaxy sample used in Fig. 2 (represented by the contours) to show the relationship between stellar population parameter errors and quality of corresponding luminosity-weighted galaxy spectra.

over the S/N range covered by the MOSES sub-sample. The quality, in terms of S/N in the g band, of the 292 host galaxy spectra of our sample is illustrated by the histogram in the lower panel of Fig. 2.

The distribution in redshift space for the full SN Ia sample is shown in Fig. 3 (open histogram) together with the redshift range covered by the MOSES sample (orange area). Only a small fraction of the SN Ia sample falls in and below the redshift range of the MOSES sample. Thus, the majority of the SN Ia host galaxies have a lower S/N than the MOSES sample (as seen in Fig. 2). It is reasonable to assume that the linear behaviour of the

error–S/N relationships can be extrapolated to lower S/N. However, at the lowest values, this may not hold such that the errors increase significantly. To avoid including data with too large uncertainties in the stellar population parameters, we cut the sample at a specific S/N value to balance the quantity and the quality of the sample. By changing the S/N limit by one unit, we find that the sample size is consistently reduced by ∼15 per cent up to S/N = 6, while above this value the sample reduction increases to >25 per cent. Hence, we only include host galaxies with S/N > 6 in the *g* band (vertical black line in the lower panel of Fig. 2). We also discover one spectrum showing quasar features and two objects with telluric contaminated Mgb absorption features. These quality cuts of the host galaxy spectra produce a final sample of 84 objects ('Host spec. quality cuts' in Table 1). We have verified that this cut in S/N does not bias the selected sample towards more luminous galaxies of higher stellar mass. The redshift distribution of this sub-sample is shown by the dash-filled histogram in Fig. 3. The final host spectroscopy sample covers redshifts up to ∼0.2. The nuisance parameters α and β from equation (1) for this sample are 0.13 and 3.29, respectively.

3 RESULTS

Relationships between host galaxy parameters age, metallicity, element ratios, velocity dispersion and stellar mass with SN Ia properties stretch factor and HR are presented in this section. We do not find any significant trends between the host galaxy parameters and SALT2 colour; hence, such relations are not further discussed.

For several of the studied relations, we derive least-squares fits. These are weighted using errors in the dependent parameter. Estimated errors of the fit parameters, derived using standard routines for least-squares fitting, are used for computing the significance of the derived fits. When stated so, the least-squares fits are sigma-clipped at a 2σ level, i.e. we first fit a line using all data points, remove the outliers deviating more than 2σ from the derived fit and finally redo the least-squares fitting using the new sample. Even though a 3σ level is more standard for sigma-clipping procedures, we noticed throughout the work that a 2σ level removed ∼5 per cent of the samples only and in several cases such a small fraction had a big impact on the derived fits. Throughout this paper, where the conclusions may be affected, we will discuss the sigma-clipped fits in relation to the non-sigma-clipped counterparts.

3.1 Emission-line diagnostics

Emission-line diagnostics are measured on the emission-line spectra separated from the galaxy absorption spectra (see Section 2.2.1). We use the emission-line EWs and amplitude-to-noise (AoN) ratios to classify each galaxy as passively evolving, star-forming or hosting an AGN. Following Baldwin, Phillips & Terlevich (1981, hereafter BPT), the ratios [O III](λ5007)/Hβ and [N II](λ6584)/Hα separate star formation and AGN activity. The AoN for [O III](λ5007), [N II](λ6584) and Hα sets the limit for emission-line detection. Due to the generally low S/N of the galaxy spectra (see Section 2.3), we allow an AoN limit of 1.5, compared to 3.0 used in Kauffmann et al. (2003b) and Schawinski et al. (2007). Hence, galaxies are classified as passively evolving if they do not have an AoN > 1.5 for [O III](λ5007), [N II](λ6584) and Hα. With this limit we find 25 out of the 84 galaxies in the final sample (see Section 2.3) to be passively evolving, i.e. 30 per cent of the SNe Ia in our sample occur in passively evolving galaxies.

Fig. 4 shows the location of the emission-line detected galaxies in the BPT diagram. The solid curved line denotes the theoretical star formation limit from Kewley et al. (2001), i.e. galaxies that fall below this line form stars. The dashed curved line shows the empirical separation of AGN and purely star-forming galaxies from Kauffmann et al. (2003b). Objects that fall between these lines are transition objects, hosting both star formation and AGN activity. For this work, we are interested in detecting star formation activity and consequently label everything below the Kewley et al. (2001) line as star-forming (blue squares). The fraction of star-forming galaxies is 41 out of 84 (∼50 per cent) and 18 galaxies are AGN (∼20 per cent, green circles). The separation of LINER and Seyfert AGNs from Schawinski et al. (2007) is also indicated by the solid straight line. Of the 18 AGN labelled galaxies, 12 are LINERs and 6 are Seyfert AGNs. The colour coding (blue = SF, green = AGN) is kept throughout this paper, adding a red colour for passively evolving objects.

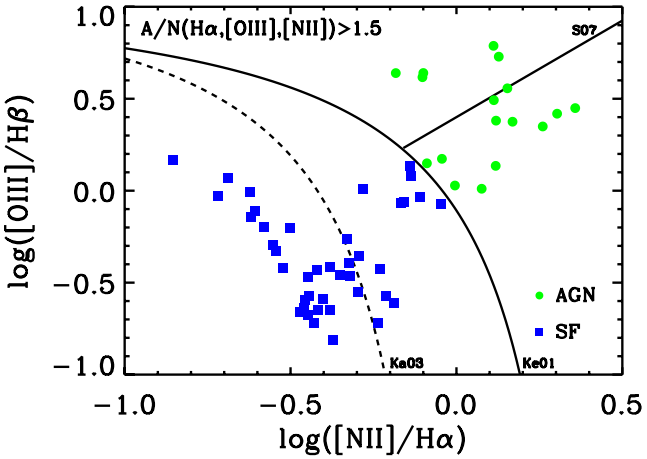

Figure 4. BPT diagram for the 59 galaxies with detected emission lines, i.e. AoN > 1.5 for Hα, [O III](λ5007) and [N II](λ6584). The blue squares denote star-forming galaxies and the green circles exhibit AGN activity only. The solid curved line shows the theoretical star formation limit from Kewley et al. (2001, Ke01) and the dashed curved line shows the empirical separation of AGN and purely star-forming galaxies from Kauffmann et al. (2003b, Ka03). Objects that fall between these lines are transition objects, hosting both star formation and AGN activity. The separation of LINERs and Seyfert AGNs from Schawinski et al. (2007, S07) is indicated by the solid straight line.

3.2 Velocity dispersion and stellar mass

In this section, we assess the stellar mass derivations and highlight ingredients in the SED fitting that are responsible for systematic uncertainties in the derived masses. This exercise is important as we will later on use stellar velocity dispersion as a proxy for stellar mass. The evaluation of the stellar mass derivations is also important since stellar mass is extensively used in the literature when studying SN Ia host galaxies.

In Fig. 5, we compare the velocity dispersion measurements from GANDALF/PPXF (see Section 2.2.1) to the various photometric stellar masses (Section 2.2.3), e.g. M05 models without reddening (M05, panel a), M05 models with reddening ($M05_{red}$, panel b), BC03 models without reddening (BC03, panel c) and BC03 model with reddening ($BC03_{red}$, panel d). A comparison between the velocity dispersion measurements and the L10 masses (see Section 2.2.3, panel e) is also included. For this sample, we find 81 out of 84 objects in common with our final sample. Data points are labelled according to the emission-line classifications from Section 3.1. Least-squares

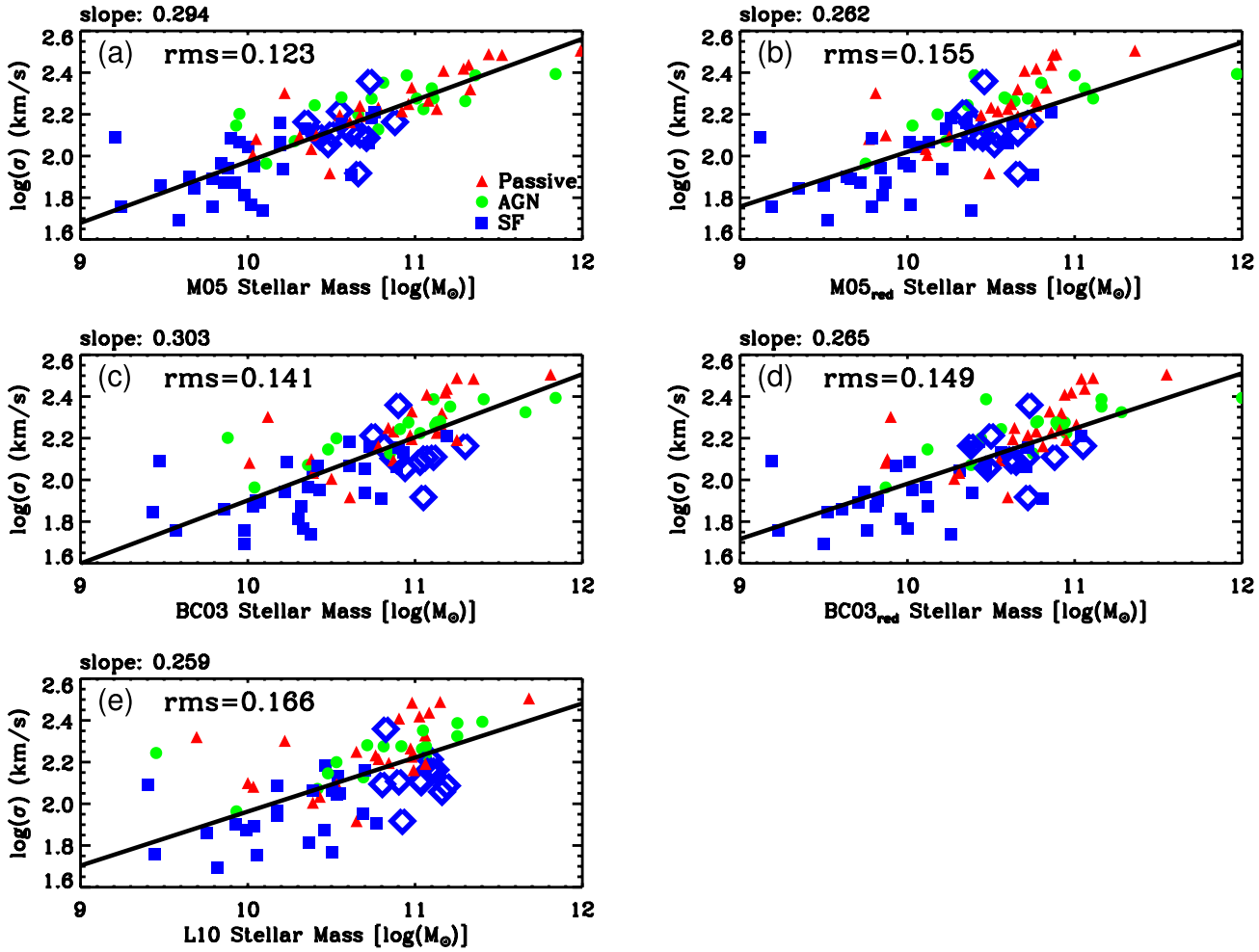

Figure 5. Comparison between stellar velocity dispersion and the different stellar masses derived in this work, i.e. M05 models without reddening (M05, panel a), M05 models with reddening ($M05_{red}$, panel b), BC03 models without reddening (BC03, panel c), BC03 model with reddening ($BC03_{red}$, panel d) and the masses from Lampeitl et al. (2010b) (L10, panel e). The data points are labelled according to their emission-line classifications from Section 3.1 and given by the labels in the upper-left panel, where passive = passively evolving, AGN = AGN activity and SF = star-forming. Least-squares fits to the σ–mass relationships are also included (solid lines) with the slopes given at the top of the panels. The standard deviations of the residuals to these fits are indicated by the labels. Star-forming galaxies with high L10 masses (lower-left panel) are highlighted as large blue diamonds in all panels, i.e. these symbols represent the same objects in all panels.

fits to the σ–mass relationships are also included in Fig. 5 (solid lines), with the slopes given at the top of the panels. The standard deviations of the residuals to these fits are indicated by the labels.

Pforr et al. (2012) make a comprehensive study of the robustness of stellar population parameters that are derived from applying SED-fitting techniques to galaxy photometry. They use mock galaxies with known input stellar mass, age, etc. and study which SED-fitting procedure is able to recover the input masses at best. They find that stellar masses are best reproduced when reddening is excluded in the SED-fitting procedure. In Fig. 5, we do indeed find the tightest correlation with velocity dispersion for the M05 case without reddening, judging from the standard deviations of the fit residuals. It can further be seen that the M05 case without reddening makes the most pronounced distinction between star-forming galaxies (blue squares) having lower masses than galaxies without emission lines, which is expected.

By comparing panels (a) and (c) in Fig. 5, we can evaluate the effect of the different models used in the SED fitting. The BC03 models produce higher masses compared to the M05 models, in particular for star-forming galaxies (blue squares). This result is well known and due to the stronger TP-AGB phase in the M05 models that contribute significantly to the luminosity of young stellar populations (see Section 2.2.3). The lower amount of near-IR light from the TP-AGB phase at intermediate ages in the BC03 models is compensated by finding a best fit at older ages, when the RGB takes over in producing near-IR light. The older age of the best fit implies then a higher M_*. In addition, the RGB takes over at older ages in the Padova tracks assumed in the BC03 models with respect to the M05 models, which contributes to the same effect (see Maraston et al. 2006 for details).

The effect of including reddening in the fit can be appreciated by comparing panel a(c) to panel b(d) in Fig. 5. In this case, the inclusion of reddening results in lower ages, hence, lower masses in particular for star-forming galaxies (see Pforr et al. 2012), a significantly larger scatter in the σ–mass relationship and consequently a flatter slope. The L10 masses are derived using reddening in the fitting procedure. These masses show a relationship with velocity dispersion similar to the BC03 with reddening case, also because

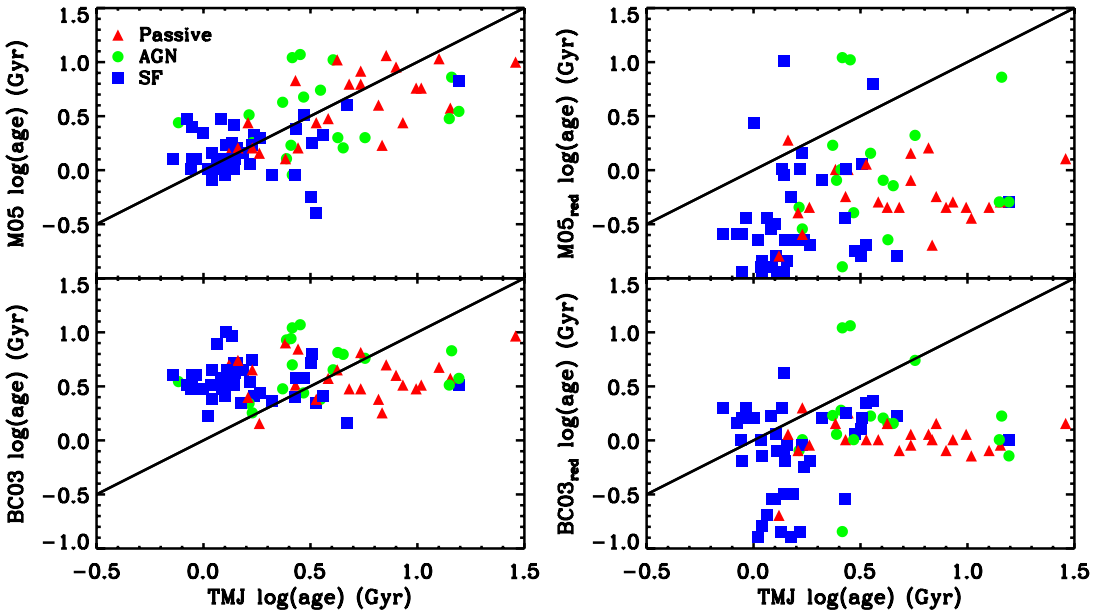

Figure 6. Comparison between ages derived using absorption line indices (TMJ, see Section 2.2.2) and the derived ages from each of the four SED-fitting cases, e.g. M05 models without reddening (M05, upper-left panel), M05 models with reddening ($M05_{red}$, upper-right panel), BC03 models without reddening (BC03, lower-left panel) and BC03 models with reddening ($BC03_{red}$, lower-right panel). The one-to-one relation is included in each of the four panels (solid lines). The data points are labelled according to their emission-line classifications from Section 3.1 and given by the labels in the upper-left panel, where passive = passively evolving, AGN = AGN activity and SF = star-forming.

of the similarity between the PÉGASE (see Section 2.2.3) and BC03 theoretical SEDs (see M05).

To emphasize the effect of choice of stellar mass derivation on star-forming galaxies, we highlight in Fig. 5 such objects that also have particularly high L10 masses, as large, open diamonds, i.e. these symbols represent the same objects in all panels. The masses for these objects shift from panel to panel and are significantly lower for the M05 cases compared to BC03 and L10.

In Fig. 6, the ages derived using absorption line indices (TMJ, see Section 2.2.2) are compared to those derived from each of the four SED-fitting cases, e.g. M05 models without reddening (M05, upper-left panel), M05 models with reddening ($M05_{red}$, upper-right panel), BC03 models without reddening (BC03, lower-left panel) and BC03 models with reddening ($BC03_{red}$, lower-right panel). The one-to-one relation is shown in each of the four panels (solid lines). The best agreement with the TMJ ages is found for the M05 case without reddening. This is also the case that shows the strongest correlation with velocity dispersion (see Fig. 5). The effect of model choice (compare the upper-left to the upper-right panel) is such that the BC03 models produce older ages for star-forming galaxies when compared to the TMJ ages. This result is due to the TP-AGB phase as already explained. The inclusion of reddening in the SED fitting leads to an underestimation of the ages (compare the left- to the right-hand panels) with respect to those derived from absorption line indices.

Note that the agreement between TMJ ages and M05 SED-fit ages is remarkable and not simply due to the fact that the underlying population model is the same. Indeed, the results of SED fit with reddening are in disagreement in spite of the use of the same model. This good result between photometrically derived and optical absorption derived ages is not found by Hansson, Lisker & Grebel (2012) in comparing ages from Lick indices from Gallazzi et al. (2005) based on BC03 models and SED fit based on the same models.

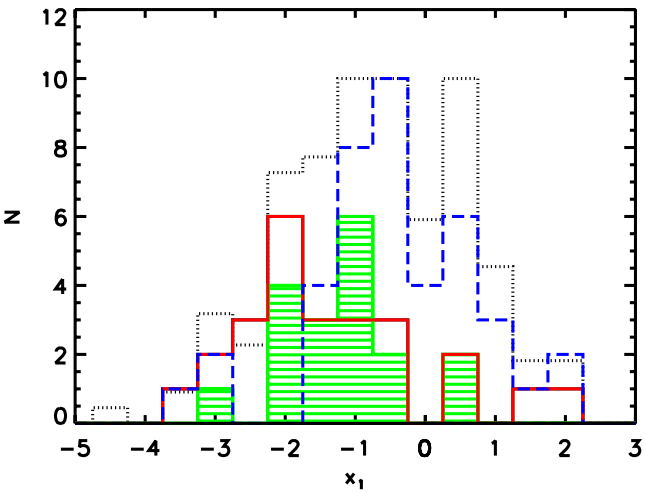

Figure 7. Distribution of the stretch factor x_1 for the different emission classifications (see Section 3.1). The blue (dashed open) histogram represents star-forming, the green (filled) represents AGN and the red (solid open) represents passively evolving galaxies. The dotted histogram shows a sample of objects with $z < 0.21$, but without the separation and host spectroscopy cuts applied, normalized to peak at $N = 10$.

3.3 Stretch factor and stellar populations

3.3.1 Final host spectroscopy sample

Fig. 7 shows the distribution in stretch factor x_1 for star-forming (blue dashed histogram), AGN (green filled histogram) and passively evolving galaxies (red solid histogram), as classified according to their emission-line strengths (see Section 3.1). It is clear that SNe Ia observed in passive galaxies have the lowest x_1 values hence the shortest decline rates, i.e. star-forming galaxies contain the most luminous SNe Ia. SNe Ia observed in galaxies with AGN activity

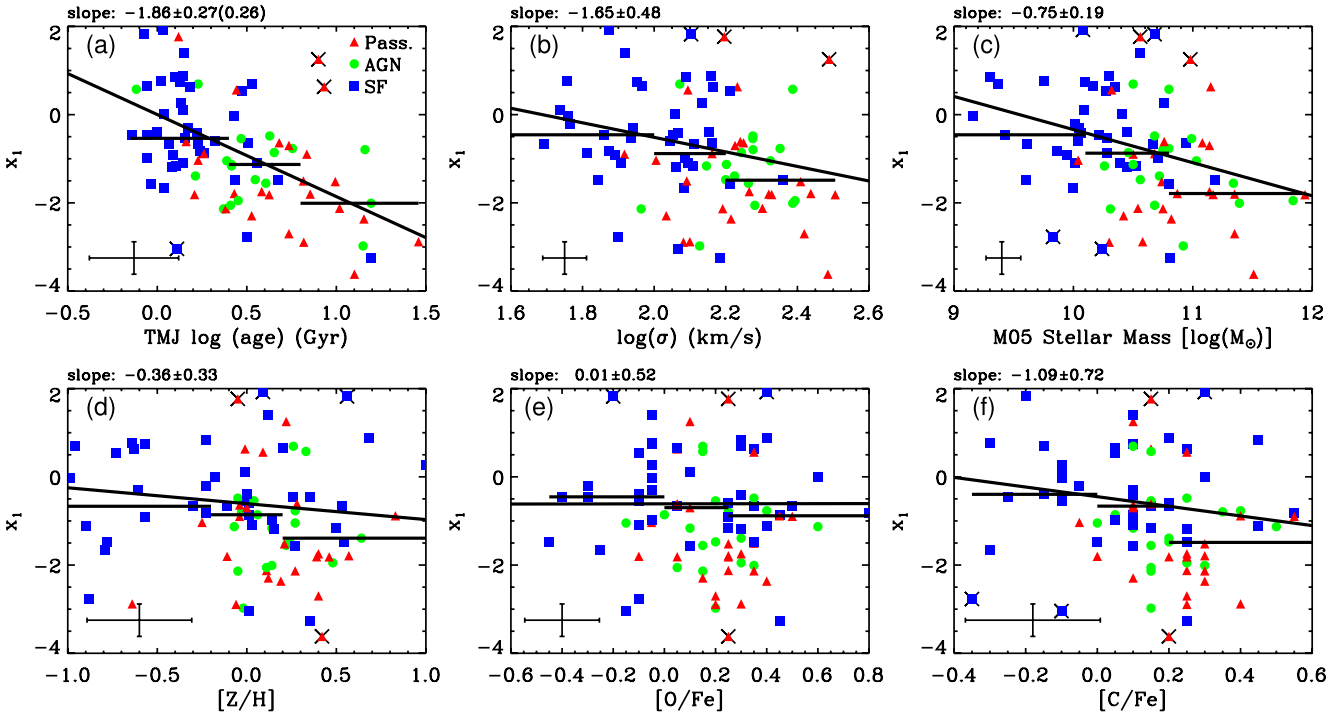

Figure 8. Relationship with host galaxy age (TMJ, panel a), velocity dispersion (panel b), stellar mass (M05 without reddening case, panel c), *Z*/H (panel d), O/Fe (panel e) and C/Fe (panel f) for the SALT2 stretch factor x_1. The data points are labelled according to the emission-line classification of the host galaxies from Section 3.1, i.e. blue squares = SF, green circles = AGN and red triangles = passively evolving. The solid lines denote one time sigma-clipped (2σ level) least-squares fits and the overplotted crosses denote removed data points. The slopes of the fits are given at the top of the panels. The value in parentheses in panel (a) is an additional error estimate for the slope (see the text for detail). The horizontal lines denote median x_1 values in bins of the *x*-axis parameters with lengths indicating the width of the bins. The error bars in the lower-left corners are average 1σ errors.

appear to have x_1 values falling in between those with star-forming and passively evolving host stellar populations. In Fig. 7, we have also included a sample of objects with redshifts <0.21, but without the separation and host spectroscopy cuts applied (see Section 2.3, dotted histogram, normalized to peak at $N = 10$). These cuts induce a mild bias towards lower x_1 values.

Relationships between the stellar population parameters (TMJ age, *Z*/H, O/Fe and C/Fe), velocity dispersion and stellar mass with SALT2 stretch factor x_1 are presented in Fig. 8. The data points are labelled according to the emission-line classification of the host galaxies from Section 3.1. The stellar masses are from the M05 without reddening case, since they showed the best agreement with stellar velocity dispersion (see Section 3.2). The solid lines represent sigma-clipped least-squares fits (removing three to five objects; see beginning of Section 3). The slope and corresponding errors of the fits are given at the top of the panels, and sigma-clipped data points are indicated by overplotted crosses. The horizontal lines denote median values in bins of the *x*-axis parameters, where the length of the lines indicates the width of the bins. Mean 1σ errors are shown by the error bars in the lower-left corners.

Clear anticorrelations between the stretch factor and stellar population age (panel a, Fig. 8), galaxy velocity dispersion (panel b) and stellar mass (panel c) are found. Hence, higher stretch factors, i.e. more luminous SNe Ia, are found in younger stellar populations and lower stellar masses. We find the slopes of the least-squares fits to be different from zero at a $>6\sigma$, 4σ and $>3\sigma$ level for the x_1–log(age), x_1–mass and $x_1 - \log(\sigma)$ relationships, respectively. The fits are weighted with the x_1 errors. However, in panel (a) the errors in age seem to dominate the scatter. To evaluate the estimated error on the fitted slope in the x_1–log(age) relation, we perturb the sample using errors in both x_1 and age through 1000 Monte Carlo simulations. For each realization, we perform a least-squares fit and determine the standard deviation of the derived set of slopes. This value is given in parentheses in panel (a) and is very close to the original error estimate.

The stretch factor also anticorrelates with *Z*/H (panel d, Fig. 8) and C/Fe (panel f), but these relations are significantly weaker than those for age, mass and velocity dispersion. The slopes of the least-squares fits are shallower and differ from zero at less than a 1σ level for *Z*/H and at a 1.5σ level for C/Fe. The x_1–O/Fe relation (panel e, Fig. 8) is flat with a large error on the fitted slope.

To summarize, out of the parameters studied, the stretch factor seems to primarily depend on the age of the host galaxy stellar populations. This age dependence is well in line with the correlation with the star formation fraction discussed above.

Using the method described in Section 2.2.2, we also derive the stellar population parameters N/Fe, Mg/Fe, Ca/Fe and Ti/Fe. We find no strong correlations for x_1 with these parameters that would add valuable information to the analysis. Measurements of N/Fe, Ca/Fe and Ti/Fe require higher S/N than the other parameters, while the derived Mg/Fe and O/Fe ratios follow each other closely (Johansson et al. 2012). Hence, we do not further discuss these abundance ratios.

3.3.2 Stacked spectra

Due to the low S/N of the individual spectra used in the previous section, in the following analysis we perform consistency checks by using stacked spectra with relatively high S/N. We stack the spectra

of the final sample in bins of x_1. Hence, in practice we stack spectra of similar galaxy class because of the correlation between x_1 and emission-line classification (see the previous section). The spectra are first de-redshifted using the SDSS spectroscopic redshifts and linearly interpolated to the same wavelength binning. We then normalize to the median flux density (f_λ) contained in the rest-frame wavelength range 5000–5500 Å. The stacking is finally performed by taking the median flux density value in each wavelength pixel (Lee et al. 2010). Using the median value is a safeguard against contaminated data, telluric contamination and features of individual spectra, and does not bias against the very highest S/N spectra. Following Lee et al. (2010), we estimate the error in each pixel of the median stacked spectra with

$$(\mathrm{S/N})_s = \sqrt{\sum (\mathrm{S/N})_i^2}, \quad (6)$$

where $(\mathrm{S/N})_s$ is the S/N of the stacked spectrum and $(\mathrm{S/N})_i$ is the S/N of the individual spectra.

The x_1 range covered by the final sample (see Section 2.3) is divided into four bins, chosen to include over a dozen number of data points in each bin. The left-hand panel of Fig. 9 shows the widths of the bins separated by the dashed horizontal lines, together with the corresponding number of objects in each bin. The histogram is the x_1 distribution for the final sample. The procedures applied to the individual spectra to compute the stellar population parameters (see Sections 2.2.1 and 2.2.2) are then applied to the stacked spectra.

The right-hand panel of Fig. 9 shows the stacked spectrum for each bin, following the colour coding of the left-hand panel. The $E(B-V)$ values produced by GANDALF/PPXF (see Section 2.2.1) for each stacked spectrum are given by the labels with corresponding colours. The stacked spectra show a number of distinct features and emission lines that clearly change as a function of the stretch factor. The largest stretch factors are found in host galaxies with the most pronounced star formation activity and the highest dust extinction. The host galaxies of faint SNe with small stretch factors, instead, are emission line free and dust free, and show strong absorption features in their spectra.

An analogue to Fig. 8, Fig. 10 shows the relationships between the stretch factor and stellar population properties and galaxy velocity dispersion for the stacked spectra. The data points in each panel are coloured according to Fig. 9 and the vertical bars indicate the size of the bins. The x_1 values are the mean within each bin. 1σ error bars are shown for each data point in the horizontal direction. The 1σ errors are similar for log (age), [Z/H], [O/Fe] and [C/Fe], i.e. smaller than 0.1 dex. The least-squares fits to the final sample from Section 3.3.1 are included for comparison (dashed lines). The horizontal range covered in each panel has been truncated compared to Fig. 8 to better resemble the parameter range covered by the data of the stacked spectra.

Lower x_1 values show older ages (panel a, Fig. 10), higher velocity dispersions (panel b) and higher total metallicities (panel d), in agreement with the case of the individual spectra (see Section 3.3.1). However, only for age (panel a) we see this trend clearly for all data points adjacent in x_1 space and significantly above the 1σ error level. For total metallicity, the trend with x_1 is diminished by the error bar overlap, which is due to the short range covered by this parameter (∼0.1 dex). A short parameter range is also found for [O/Fe] (∼0.1 dex, panel e, Fig. 10) and [C/Fe] (∼0.1 dex, panel f), resulting in a significant error bar overlap. We see no clear trends for these parameters. Hence, the result of the individual spectra from Section 3.3.1 is reproduced for the stacked spectra, i.e. x_1 show the strongest dependence on stellar population age.

3.3.3 *Comparison with the literature*

In agreement with Oemler & Tinsley (1979), van den Bergh (1990), Mannucci et al. (2005), Sullivan et al. (2006) and Smith et al. (2012), we find a higher fraction of SN Ia events in star-forming compared to passively evolving galaxies. Star-forming galaxies also show slower decline rates, i.e. more luminous SNe Ia, compared to passively evolving galaxies, a pattern first noticed by Sullivan et al. (2006) and further confirmed by Howell et al. (2009), Neill et al. (2009), L10 and Smith et al. (2012). For the first time, we

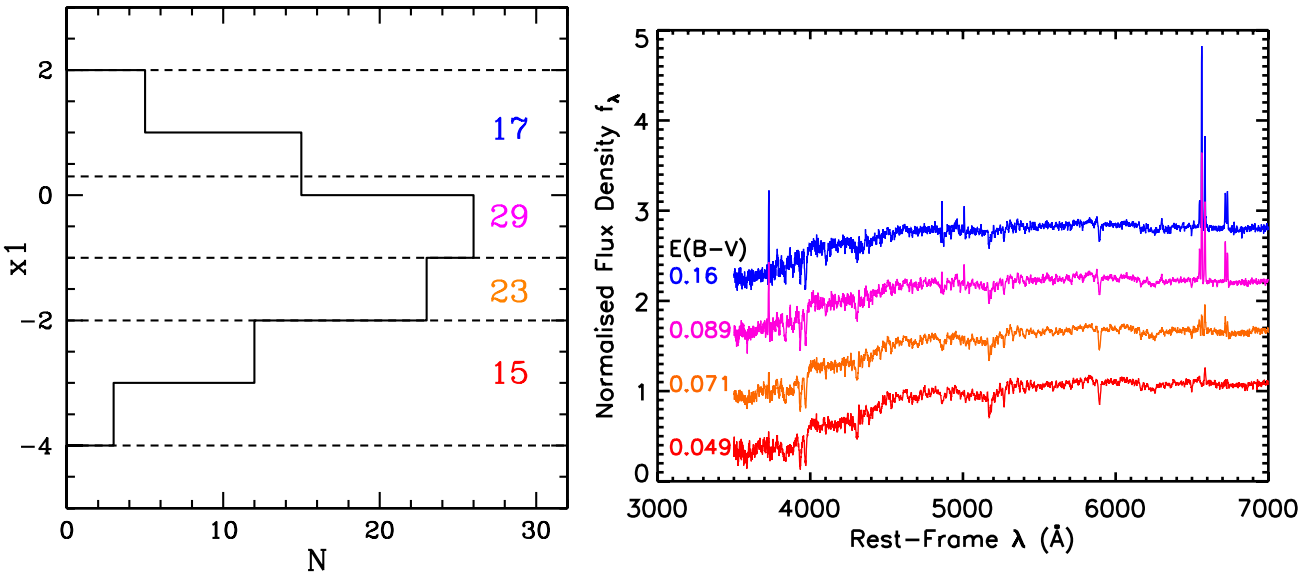

Figure 9. Left-hand panel: binning in x_1 for stacking of spectra, where the limits of the bins are indicated by the horizontal dashed lines. Coloured labels state the number of objects within each individual bin. The histogram is distribution of x_1. Right-hand panel: resulting stacked spectra at rest-frame wavelength and for normalized flux density per unit λ (f_λ), coloured according to the bin labels of the left-hand panel. The labels, with corresponding colours, state the $E(B-V)$ value for each stacked spectrum.

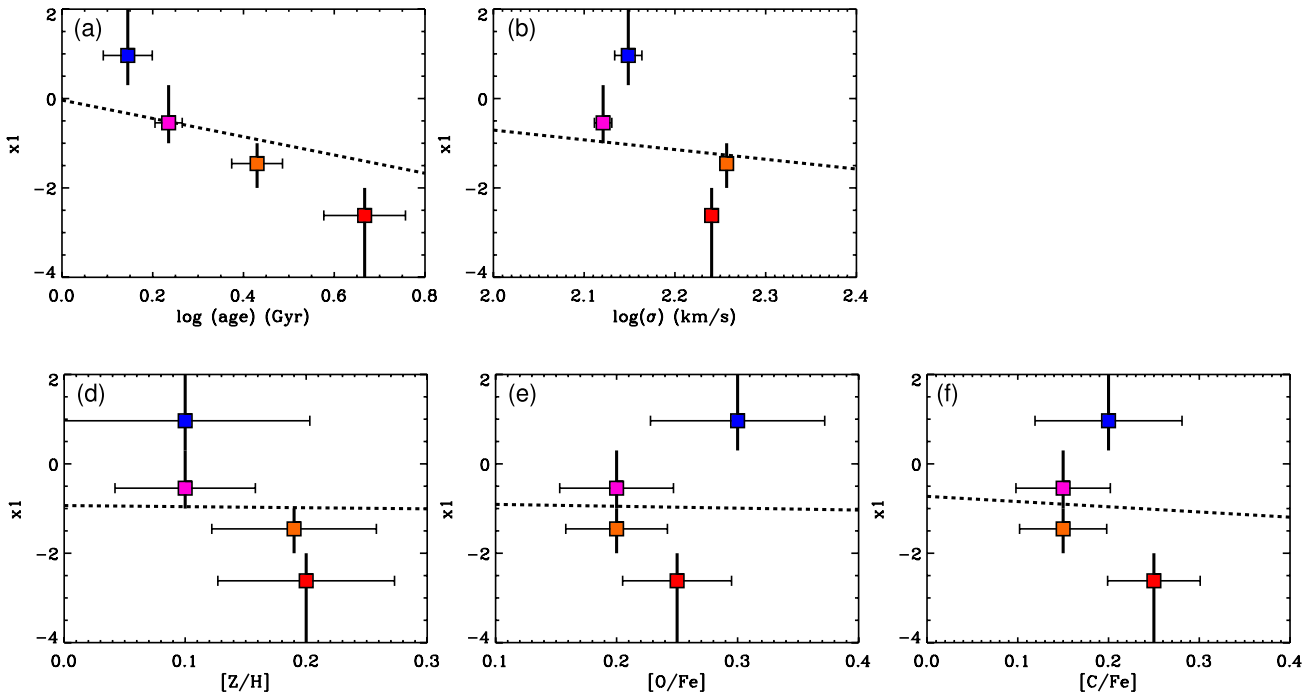

Figure 10. Relationship with host galaxy age (panel a), velocity dispersion (panel b), *Z*/H (panel d), O/Fe (panel e) and C/Fe (panel f) for SALT2 x_1 for the stacked spectra. The data points are coloured according to the colours of the binned spectra in Fig. 9. The 1σ errors for the x-axis parameters are indicated by the horizontal error bars and bin widths are shown by the vertical bars. The x_1 value for each data point is the average x_1 value in the corresponding bin. The dashed lines denote the least-squares fits for the corresponding relationships of the individual spectra from Fig. 8.

establish an anticorrelation between the host galaxy velocity dispersion and stretch factor, suggesting faster decline rates in more massive galaxies. A similar anticorrelation is also found for stellar mass, in agreement with Howell et al. (2009), Neill et al. (2009) and Sullivan et al. (2010).

For stellar metallicity and element abundance ratios, we instead only find weak SALT2 x_1 dependences.

Furthermore, we find a clear anticorrelation between the stretch factor and luminosity-weighted stellar population age which is more prominent and well defined than found for velocity dispersion and stellar mass. This result indicates that the x_1–mass relationship is a result of the correlation between galaxy mass and stellar population age.

Hamuy et al. (2000) and Gallagher et al. (2008) investigated absorption line indices allowing for distinction between age and metallicity effects. The former prefer metallicity over age as the main driver of SN Ia luminosity using only five objects. Gallagher et al. (2008) studied 29 SN Ia host galaxies and found age to be the dominant stellar population parameter affecting SN Ia luminosity. Two recent studies, Howell et al. (2009) and Neill et al. (2009), derived host galaxy parameters from photometry. Both authors favour age over metallicity as the SN Ia luminosity-dependent factor, but determine the latter only indirectly by using derived masses and the mass–metallicity relationship from Tremonti et al. (2004). Brandt et al. (2010) found high-stretch SNe Ia in young stellar populations (<400 Myr) and low-stretch SNe Ia in old stellar populations (>2.4 Gyr). In a recent study, Gupta et al. (2011) found faster decline rates for older stellar populations using photometry, but did not include metallicity or element abundance ratios in their study.

To conclude, this analysis strengthens the emerging trend in the literature that host stellar population age is the main driver of SN Ia LC shape and luminosity, such that more luminous SN Ia events occur in galaxies with younger stellar populations.

3.4 HR and stellar populations

3.4.1 Final host spectroscopy sample

Fig. 11 shows HR as a function of stellar population age (panel a), [*Z*/H] (panel d), [O/Fe] (panel e), [C/Fe] (panel f) and velocity dispersion (panel b) for the final host spectroscopy sample. The same colour coding and symbols as in Fig. 8 are used. We do not find significant trends for any of the parameters studied ($<2\sigma$ level for all parameters, regardless of applying sigma clipping or not). To be sure that the quality of the host spectra does not dilute possible trends, we have also stacked the spectra in two HR bins dividing the sample into sub-samples of roughly equal sizes. The stacking follows the procedure described in Section 3.3.2. Table 3 presents the HR range, number of objects and mean HR for the two bins, together with the stellar population parameters and velocity dispersion derived for the stacked spectra. We do not find significant differences for any of the stellar population parameters as well as for velocity dispersion between the two bins.

The relationship between HR and gas-phase metallicity (see Section 2.2.4) is presented in Fig. 12 (left-hand panel). As pointed out in Section 2.2.4, AGN activity may affect the derived metallicities. The gas-phase metallicities are thus shown for galaxies with detected emission lines and classified as star-forming. Galaxies in the transition region between star formation and AGN activity (see Section 3.1) are plotted as open symbols. Least-squares fits are derived for all data points (solid line) and purely star-forming galaxies (solid points, dashed line) with slopes given by the labels. Since this is a small sample, we do not sigma-clip the least-squares fits.

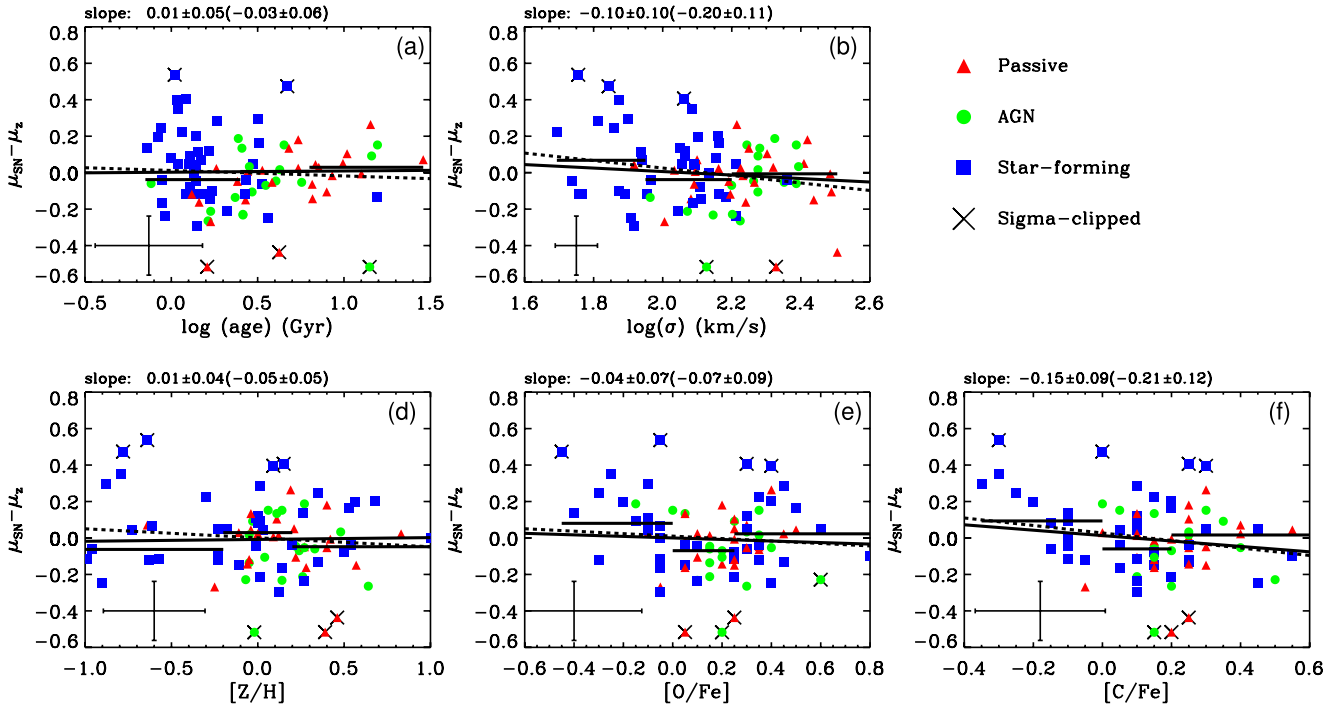

Figure 11. Relationship with stellar population age (panel a), velocity dispersion (panel b), [*Z*/H] (panel d), [O/Fe] (panel e) and [C/Fe] (panel f) for HR. The data points are labelled according to the emission-line classification of the host galaxies from Section 3.1, i.e. blue squares = SF, green circles = AGN and red triangles = passively evolving. The solid and dashed lines denote least-squares fits with and without one time sigma clipping (2σ level), respectively. The overplotted crosses denote removed data points for the sigma-clipping cases. The slopes and corresponding errors are given at the top of the panels (in parentheses for the non-sigma-clipping cases). The horizontal lines denote median HR in bins of the *x*-axis parameters with lengths according to the width of the bins. The error bars in the lower-left corners are average 1σ errors.

Table 3. Stellar population parameters for stacked spectra in bins of HR. The stacking limits are given in column 1, the number of objects in each stack in column 2 and the mean HR in column 3. The stellar population parameters together with corresponding errors are given in columns 4–7 and velocity dispersion in column 8.

Stack	*N*	⟨HR⟩	log(age) (Gyr)	[Z/H]	[O/Fe]	[C/Fe]	σ (km s^{-1})
HR > −0.05	43	0.13	0.44 ± 0.04	0.08 ± 0.06	0.30 ± 0.05	0.25 ± 0.05	148.2 ± 2.5
HR < −0.05	41	−0.16	0.33 ± 0.04	0.10 ± 0.06	0.25 ± 0.05	0.20 ± 0.05	152.9 ± 2.3

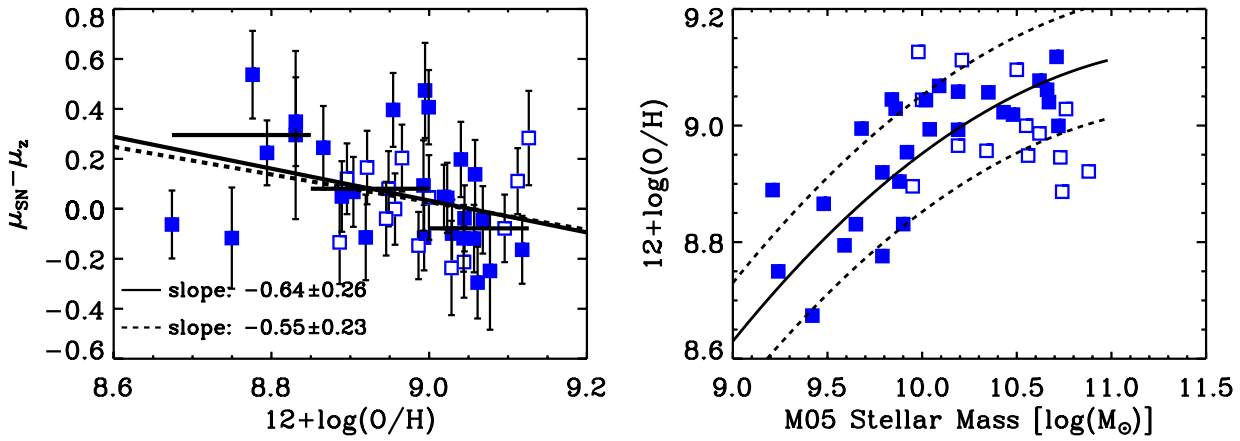

Figure 12. Left-hand panel: relationship between gas-phase metallicity and HR for purely star-forming galaxies (blue solid points) and transition galaxies (open blue points). The solid line and the dashed line denote least-squares fits to all data points and to solid data points, respectively. The slopes and corresponding errors are given by the labels. The horizontal lines denote median HR in bins of the *x*-axis parameters with lengths according to the width of the bins for all data points. Right-hand panel: relationship between gas-phase metallicity and stellar mass; the same symbols as in the left-hand panel. The solid curve shows the relation from Tremonti et al. (2004) with 1σ errors (dashed curves).

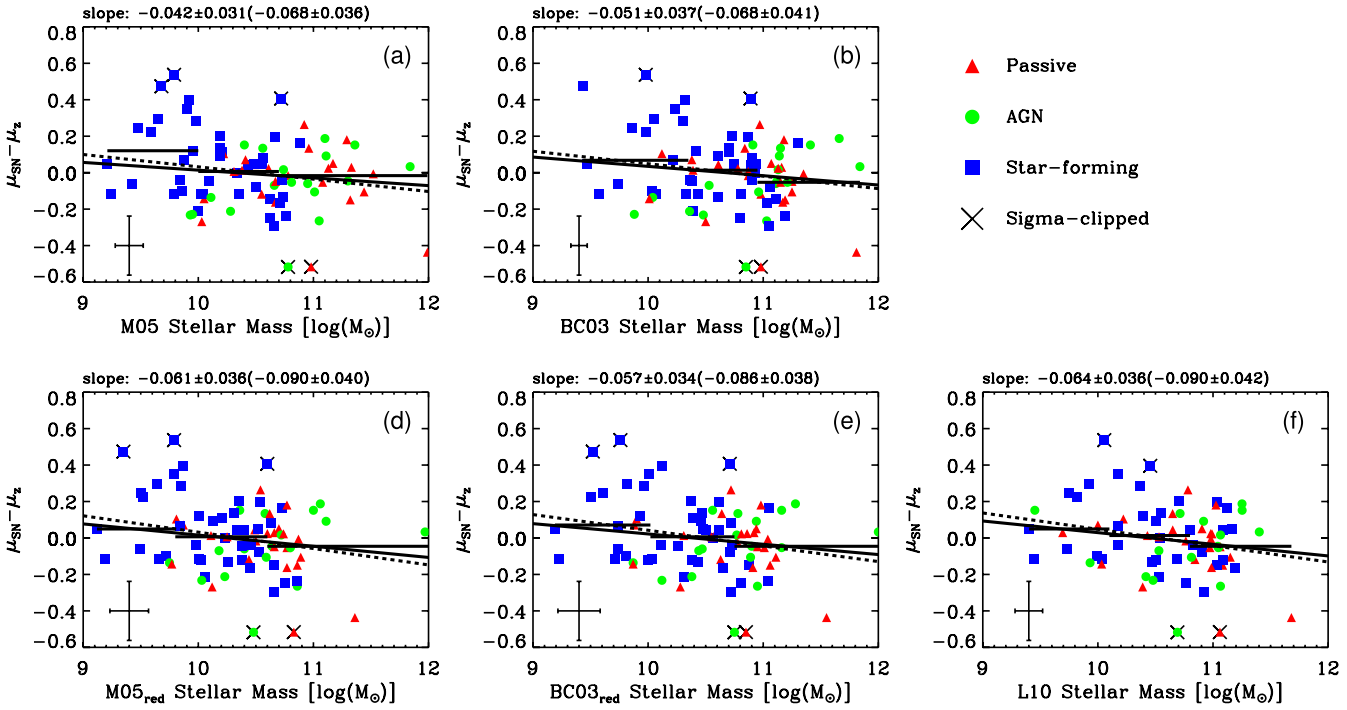

Figure 13. Relationship between HR and the stellar masses derived for the different prescriptions described in Section 2.2.3, e.g. M05 models without reddening (M05, panel a), M05 models with reddening ($M05_{red}$, panel d), BC03 models without reddening (BC03, panel b), BC03 model with reddening ($BC03_{red}$, panel e) and masses from Lampeitl et al. (2010b) (L10, panel f). The data points are labelled according to the emission-line classification of the host galaxies from Section 3.1, i.e. blue squares = SF, green circles = AGN and red triangles = passively evolving. The solid and dashed lines denote least-squares fits with and without one time sigma clipping (2σ level), respectively. The overplotted crosses show removed data points for the sigma-clipping cases. The slopes and corresponding errors are given at the top of the panels (in parentheses for the non-sigma-clipping cases). The horizontal lines denote median HR in bins of the x-axis parameters with lengths according to the width of the bins. The error bars in the lower-left corner are average 1σ errors.

Median values in bins of metallicity are shown for all data points as horizontal lines. These lines show a tentative trend of decreasing HR for higher gas metallicities. The least-squares fits also indicate a decrease in HR with gas-phase metallicity, but with a low significance of $<2.5\sigma$.

Several previous studies claim that gas-phase metallicity should be used to further minimize the scatter in the HR (D'Andrea et al. 2011; Hayden et al. 2013). Our results only tentatively strengthen gas-phase metallicity to be a main driver of this scatter. The low statistical significance of the derived relation is affected by the two low-metallicity, low-HR data points. Considering the individual HR errors, both points deviate more than 2σ from the least-squares fits. Ignoring the two outliers in the least-squares fitting results in a significantly steeper slope of -1.05 ± 0.28, hence, with a higher statistical significance. This is done under the assumption, based on the previous work, that a fundamental relation between gas-phase metallicity and HR exists. One possible explanation for the two outliers could be a failure in the emission-line template fitting (see Section 2.2.1), affecting the derived gas-phase metallicities. However, this is not the case for either of the two objects. We have further studied the location of these SN events with respect to the SDSS fibre location of the host galaxy. For the lowest metallicity object, the SN event is within the SDSS aperture and it is a spectroscopically confirmed Ia. The other outlier object, not spectroscopically confirmed Ia, is located in the outskirts of the galaxy, at a distance of about two times the SDSS aperture diameter (3 arcsec) from the fibre centre. This could possibly explain the deviation of this object if a significant positive gas-phase metallicity gradient or a local metallicity upturn is present. It should be emphasized that our results only tentatively strengthen gas-phase metallicity to be a main driver of the scatter in the HR and that a lack of a fundamental relation between gas-phase metallicity and HR is a possibility.

It is important to ensure that the derived metallicities are robust. The relationship between gas-phase metallicity and stellar mass is shown in the right-hand panel of Fig. 12. The relation from Tremonti et al. (2004) is also shown together with 1σ errors. We conclude that our relationship is in very good agreement with that of Tremonti et al. (2004) and that our derived metallicities are well behaved. In particular, the two outlier points in the relation between gas-phase metallicity and HR do not appear to be underestimated.

Fig. 13 shows the relationship between HR and the stellar masses derived for the different prescriptions described in Section 2.2.3, e.g. M05 models without reddening (M05, panel a), M05 models with reddening ($M05_{red}$, panel d), BC03 models without reddening (BC03, panel b) and BC03 model with reddening ($BC03_{red}$, panel e). The relationship between HR and the L10 stellar masses is also included (panel f). The data points are labelled, as usual, with blue squares = star-forming, green circles = AGN and red triangles = passively evolving galaxies. The solid and dashed lines represent least-squares fits with and without one time sigma clipping (2σ level, see beginning of Section 3), respectively. The overplotted crosses denote removed data points for the sigma-clipping cases. The slopes and corresponding errors are given at the top of the panels (in parentheses for the non-sigma-clipping cases). The horizontal lines show median values in bins of the x-axis parameters, where the length of the lines indicates the width of the bins.

We can see in Fig. 13 that the method of stellar mass derivation affects the HR–mass relationship. The masses derived with the M05

models without reddening show the weakest trend with HR and hence the smallest difference in HR for high- and low-mass objects. These masses also showed the strongest correlation with velocity dispersion in Section 3.2. In comparison, the masses derived with reddening display stronger trends with HR, similar to the trend for the L10 masses. This dependence on stellar mass derivation is present also when sigma clipping (see beginning of Section 3) is not applied. In this case, all trends become significantly steeper; hence, only a handful of objects (∼5 per cent) affect the trends.

3.4.2 Extended photometric sample

In addition to the SNe Ia with both available host galaxy SDSS spectroscopy and photometry, we can add SNe Ia with available SDSS photometry only to extend the sample for studying stellar masses. For this purpose, we add the sample studied in L10. These authors made a number of quality, redshift and host galaxy-type cuts that produced a sample of 162 objects. We followed the quality cuts of L10 for the host spectroscopy sample studied in this work, but we have also applied further quality cuts as described in Section 2.3. These additional constraints are lifted here in order to have a homogeneous sample. Specifically, the cut in S/N of the host galaxy spectra can be removed when we focus on photometry only. For the purpose of having a homogeneous sample, we now also apply the redshift cut from L10, i.e. selecting objects with $z < 0.21$. In fact, the S/N cut of the final host spectroscopy sample removed objects with $z > 0.21$ (see Fig. 3).

The host galaxy-type cut in L10 was made in order to be able to study two distinct types of host galaxies, passive and star-forming, by constraining the allowed error on derived SFRs. Since we are not interested in distinct types of galaxies in this work, we can ignore this cut. The host spectroscopy sample used in our study is drawn from the same parent sample as the L10 sample; we will therefore mainly just add galaxies rejected due to the galaxy-type cut in L10. This action results in a sub-sample of 145 objects drawn from the full host spectroscopy sample. Out of this sub-sample, 60 are in common with the L10 sample, leaving a Master photometric sample consisting of 247 objects.

We have derived the HR independently for each of the different samples. The α and β values from equation (1) for each of these fits are presented in Table 4 for the host spectroscopy sample (Spec.), the Master sample and the L10 sample. The values for the final selection sample (Final) used in the previous sections are also included for comparison. We have also derived the HR including $z > 0.21$ galaxies for the host spectroscopy sample and the Master sample. The α and β values are consistent for all samples as the 1σ errors are typically 0.02 and 0.2, respectively (L10). We find small variations only in the HR derived for the different samples, considering objects in common between the samples.

Table 4. The values of α and β from equation (1) for the different samples used throughout the paper.

Sample	α	β
Final	0.13	3.29
Spec.	0.12	3.40
Spec. (incl. $z > 0.21$)	0.14	3.18
Master	0.12	3.21
Master (incl. $z > 0.21$)	0.13	3.08
L10	0.11	2.97

Fig. 14 presents HR as a function of host stellar mass, derived with the M05 without reddening option, for the Master sample. The sub-samples are indicated by blue triangles for the L10 sample and red circles for the host spectroscopy sample. The open, red filled blue squares denote overlapping objects. All points represent HR derived for the Master sample, and the black dashed line represents the corresponding least-squares fit. The cyan horizontal lines denote median HR values for the Master sample, in bins of mass with lengths according to the width of the bins.

Least-squares fits are derived for the HR computed for each of the samples and for the different mass derivations, with slopes presented in Table 5. Each sample was sigma-clipped twice at a 2σ level, where each clip removes ∼5 per cent of the sample size. The values in parentheses in Table 5 are slopes without any sigma clipping. The fit to the Master sample is more or less unaffected by the sigma clipping, while the two sub-samples are severely affected by the removal of only a fraction of the samples. Hence, the σ-clipped fits are better representatives of the bulk of data points. In both cases, the slope of the Master sample lies in between the values of the two sub-samples. For the L10 sample, we recover the trend found in L10, but with a steeper slope when sigma clipping is adopted. The systematic variations due to stellar mass derivation, apparent for the smaller sample (see Section 3.4.1), are weaker but still present when the number of objects is increased. It should be mentioned that the Master and host spectroscopy samples lack L10 masses for ∼10 per cent of the objects. Hence, the fits for those samples and masses are not directly comparable to the others.

Two effects are responsible for the variation in slope of the different samples. (1) The median HR values (cyan horizontal lines in Fig. 14) show a drop around $\log M_{\odot} = 10.0$ and are close to constant below and above this value. (2) The L10 and host spectroscopy samples have different stellar mass distributions, which is apparent in Fig. 14. This is better emphasized in Fig. 15, where the top panel shows the stellar mass distributions for the different samples, i.e. blue dot–dashed and red histograms represent the L10 and host spectroscopy samples, respectively. The host spectroscopy sample is lacking low-mass objects, due to the SDSS magnitude selection cut for spectroscopy (see Sections 2). The L10 sample is instead deficient in high-mass galaxies, due to the removal of, typically high-mass, galaxies with uncertain classifications in L10 (see their fig. 1). The high-mass bias of the host spectroscopy sample is not surprising as SDSS spectroscopic targeting required a magnitude of $r < 17.7$ for the main galaxy sample (Strauss et al. 2002).

The discrepancy in slope between the different samples is driven by the different mass ranges covered. This result is shown in the main panel of Fig. 15, which is a remake of Fig. 14. Here we instead study the HR distributions in three different mass intervals, following the behaviour of the cyan lines in Fig. 14: $\log M_{\odot} < 9.5$, $9.5 < \log M_{\odot} < 10.2$ and $\log M_{\odot} > 10.2$. Least-squares fits, derived without the cyan diamond-shape points, in these different regions are presented by the lines with slopes according to the labels in the corresponding mass intervals. For the high-mass bin, the HR–mass relation is clearly flat. This appears to be the case also for the low-mass bin, but this regime is more sparsely populated. Higher HR are found at low masses, while in the region around $\log M_{\odot} \sim 10.0$, the HR varies significantly. Hence, the HR–mass relationship shows the behaviour of a sloped step function where negative and positive values are found for high- and low-mass objects, respectively. A similar behaviour of the HR–mass relation can also be found in the sample studied in Sullivan et al. (2010). It is clear from their fig. 4 that the HR suddenly drop above $\log M_{\odot} \sim 10.0$, while above and below this limit the average HR stay roughly constant. In the recent

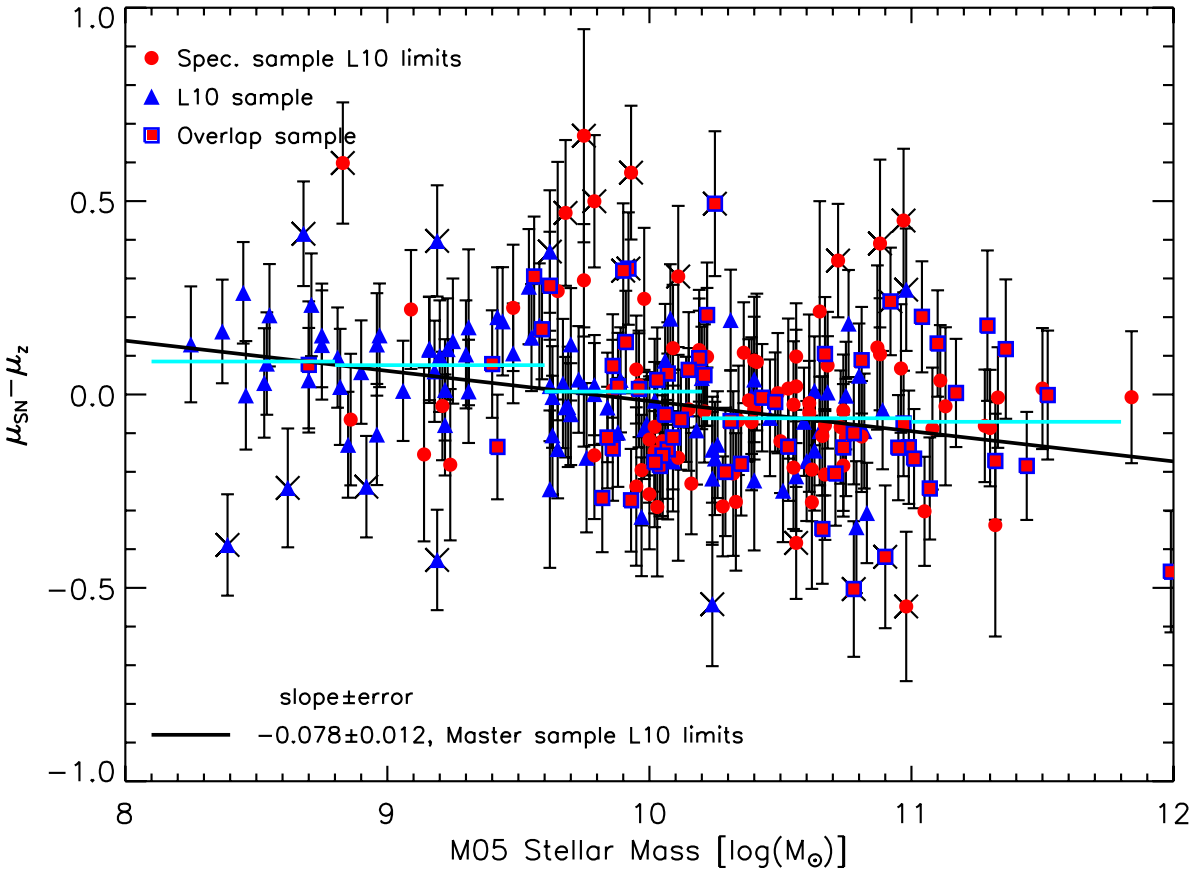

Figure 14. Relationship between HR and stellar mass for the different samples studied (see the text). The masses are derived using the M05 models without reddening (see Section 2.2.3). The different samples are indicated by the upper labels with corresponding colours and symbols, i.e. red circles = host spectroscopy sample, blue triangles = L10 sample and red filled blue squares = overlap sample. The line shows a least-squares fit to the Master sample, with a slope and error given by the lower label. The overplotted crosses denote data points removed by twice sigma clipping the Master sample. The cyan horizontal lines denote median HR values for the Master sample, in bins of mass with lengths according to the width of the bins.

Table 5. Slopes and corresponding errors of least-squares fits for the different samples studied and different stellar mass derivations. The values in parentheses are for fits before applying the σ clipping. The last column gives the typical 1σ error in slope for each sample.

Sample	N	M05	$M05_{red}$	BC03	$BC03_{red}$	L10 (PÉGASE)	Error
Spec.	145	−0.054(−0.088)	−0.077(−0.110)	−0.055(−0.090)	−0.062(−0.106)	−0.046(−0.069)	±0.023(0.029)
L10	162	−0.088(−0.064)	−0.087(−0.077)	−0.077(−0.065)	−0.091(−0.065)	−0.082(−0.064)	±0.013(0.017)
Master	247	−0.078(−0.070)	−0.080(−0.083)	−0.070(−0.070)	−0.087(−0.073)	−0.074(−0.068)	±0.012(0.015)

work of Childress et al. (2013), a similar sloped step function of the HR–mass relation is found and where the HR also rapidly change around $\log M \sim 10.0$.

The stellar mass coverage is responsible for the sensitivity to individual points of the HR–mass relation, demonstrated above by the variation in slope when applying and not applying sigma clipping to the least-squares fitting. The Master sample has a better mass coverage and is therefore less affected, while the two sub-samples, lacking high- or low-mass galaxies, are sensitive to individual points.

Stellar masses around 10^9 $M_\odot$ may not represent the total mass of a galaxy, but the mass of the star-forming fraction, which outshines the underlying older population (the 'tip of the iceberg' effect; Maraston et al. 2010). The simulations of Pforr et al. (2012) indicate that when a 10^{11} $M_\odot$ galaxy has experienced a 1–10 per cent by mass recent starburst, the SED-fit-derived mass is closer to the mass of the burst rather than to the total mass. This effect applies to stellar masses derived from SED fitting in general and is not typical for the stellar masses derived in this work. The uncertainty at the lower mass end makes the plateau in the HR–mass diagram (see Fig. 15) in this regime dubious.

The linear fits in the high- and low-mass regimes are statistically consistent with zero slopes. Adopting the median HR for $\log M_\odot < 9.5$ (0.099 mag) and $\log M_\odot > 10.2$ (−0.067 mag), together with the linear fit for $9.5 < \log M_\odot < 10.2$, we get a four-parameter function. We test the significance of this sloped step function ($\chi^2_{red} = 1.460$ for the full Master sample) as compared to the single linear fit ($\chi^2_{red} = 1.485$) over the full mass range. We also compare to the case of using a two-parameter constant step function ($\chi^2_{red} = 1.475$), based on the median HR for $\log M_\odot < 10$ (0.039 mag) and $\log M_\odot > 10$ (−0.069 mag). The significance is tested using the resulting χ^2-values and an F-test for nested regression models. To have the same sample for all models, we use the full Master sample and take into account that the sloped step function has four parameters instead of two for the single linear fit and the

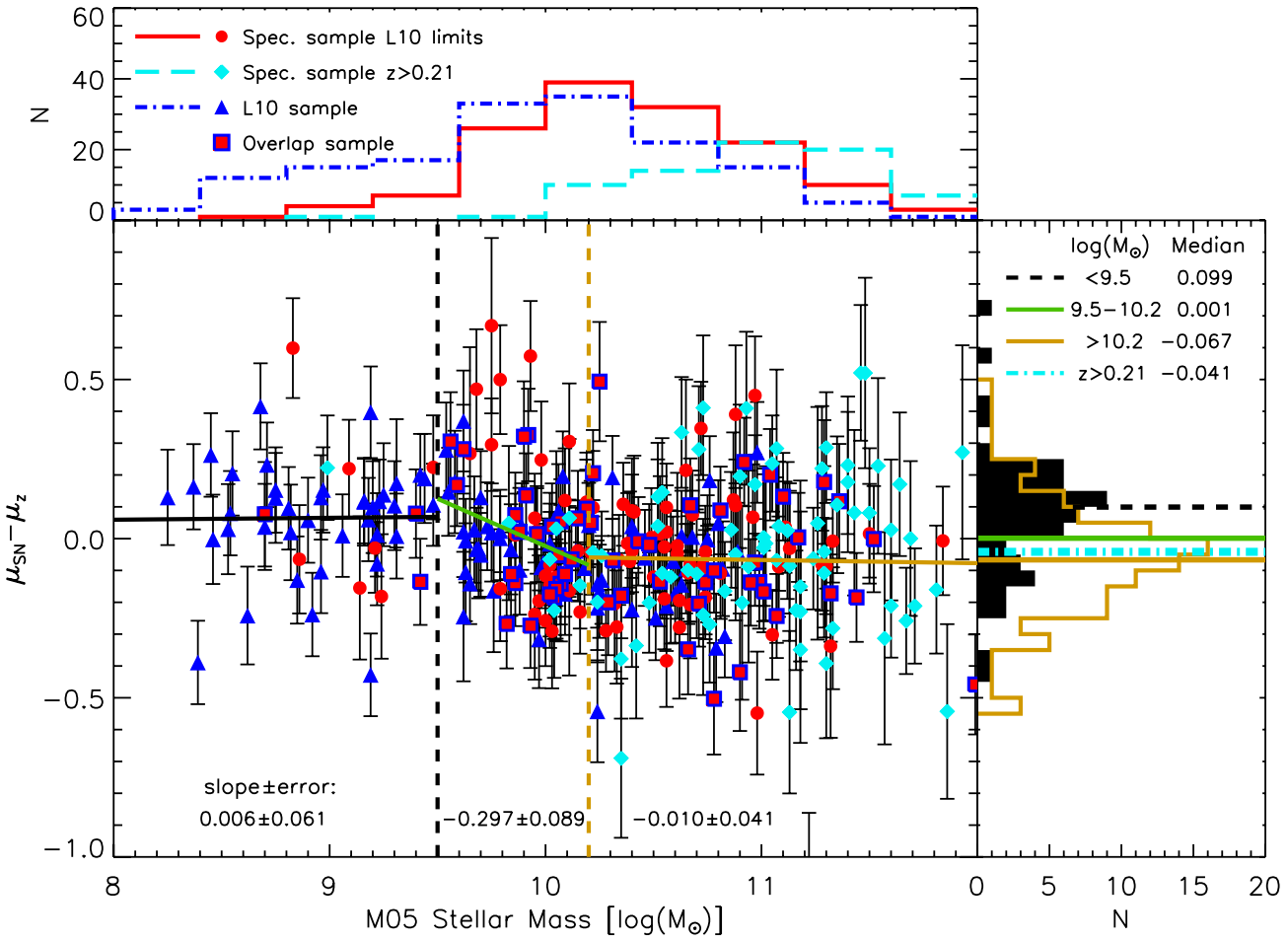

Figure 15. Upper panel: histograms of the stellar mass distribution for the different samples studied (see the text) as indicated by the labels. Main panel: remake of Fig. 14, but also adding high-redshift objects ($z > 0.21$, cyan diamonds, not used in the least-squares fits). The vertical dashed lines indicate boundaries between different mass ranges for which we derive least-squares fits. The slope of each fit is given by the labels in the different mass intervals. Right-hand panel: the HR distributions for the high (open orange histogram) and low (filled black) stellar mass bins of the main panel. The labels give the median values in each mass bin, and for the $z > 0.21$ sample, also presented by the lines of corresponding style and colour.

constant step function. We find that the *F*-test rejects the null hypothesis that the sloped step function does not provide a significantly better fit than the single linear fit and the constant step function at a probability >90 per cent and >85 per cent, respectively.

The HR distributions of the high (open orange histogram) and low (filled black) stellar mass bins are plotted in the right-hand panel of Fig. 15 with colours. The labels give the median values in each mass bin and for the $z > 0.21$ sample, also presented by the lines with corresponding style and colour. The median HR of the low-mass bin is offset from the high-mass bin by 0.166 ± 0.030 mag, while the median value of the intermediate-mass bin is located between these values. The 1σ error is derived as $(\sigma_1^2/n_1+\sigma_2^2/n_2)^{1/2}$, where σ^2 and n are the variances and sample sizes of the two distributions. A Kolmogorov–Smirnov test confirms that the distributions of the high- and low-mass bins are different at a significance level of over 99.9 per cent. Hence, the stellar mass distribution of the selected sample strongly affects the derived HR–mass trend. This would not be the case if there were a continuous trend over the full stellar mass range.

To further emphasize this point, we added the sub-sample of objects with $z > 0.21$ (cyan diamonds) in Fig. 15. The HR for this sample were derived for the Master sample including $z > 0.21$ objects. We confirm that the HR for the rest of the Master sample, i.e. $z < 0.21$ objects, are very similar to the derived values when the $z > 0.21$ objects are excluded. In the top panel, it is clear that the $z > 0.21$ sample is distributed towards high stellar masses. This sub-sample exhibits low HR similar to the high-mass bin of the Master sample, as can be seen in the main and right-hand panel.

We confirm similar sloped step functions for all stellar mass derivations, i.e. M05 with reddening, BC03 without reddening, BC03 with reddening and also for the stellar masses derived with the setup of L10. We have also applied the cuts described in Section 2.3 to the Master sample and L10 sample and find that the results are not affected. However, since the cut in spectral resolution cannot be applied to the L10 sample, it has not been considered for this consistency check.

3.4.3 *Comparison with the literature*

We find that HR depends on host galaxy mass in agreement with several recent reports in the literature (Kelly et al. 2010; L10; Sullivan et al. 2010; Gupta et al. 2011). However, we find that the HR–mass relationship behaves as a sloped step function, which can also be seen in the work of Sullivan et al. (2010) and in the recent work of Childress et al. (2013), where the HR are also found to rapidly change around $\log M \sim 10.0$. For the first time, we study

the relation between HR and stellar velocity dispersion, but find no significant trend. However, this may be due to the high-mass bias of the sample studied.

It is believed that the HR–mass trend is the result of a more fundamental relationship between HR and SN Ia progenitor properties that could possibly be mimicked through host stellar populations. Several authors have therefore also studied relationships between HR and the stellar population parameters age and metallicity. Gallagher et al. (2008) is the only study in the literature to date that is based on absorption line indices and find stellar metallicity to be the source of systematic HR variations for a small sample of ∼20 host galaxies. Howell et al. (2009) and Sullivan et al. (2010) instead infer gas-phase metallicities from stellar masses together with the mass–metallicity relationship from Tremonti et al. (2004) and find significant trends in these parameters with HR. Gas-phase metallicities are also inferred from stellar mass in a similar way by Neill et al. (2009), but they instead find a stronger relation between stellar population age and HR. Similar to this work, D'Andrea et al. (2011) derive gas-phase metallicities directly from the emission-line ratios and find a trend of higher HR in galaxies of lower metallicity. Hayden et al. (2013) find that the scatter in the HR is reduced using gas-phase metallicity derived from the fundamental metallicity relation of Mannucci et al. (2010) (defined by metallicity, stellar mass and SFR) as a further fit parameter, compared to using stellar mass or gas-phase metallicity from the mass–metallicity relation. Gupta et al. (2011) instead find stellar population age to correlate with HR. For the sample of 84 host galaxies studied in this work, we do not find significant trends of HR with any of the absorption line derived stellar population parameters age, metallicity and element ratios. Again, this may be due to the high-mass bias of the sample studied.

We have shown in the previous two sub-sections that the HR–mass trend is dependent on the mass range spanned by the galaxies. The lack of a trend between HR and velocity dispersion as well as with stellar population age and metallicity could therefore be the result of the limited mass range studied through the final host spectroscopy sample. The reason why we find a tentative relationship for gas-phase metallicity probably arises from the fact the star-forming galaxies, for which we can infer gas-phase metallicities, cover the stellar mass range where the HR dramatically vary (around 10^{10} $M_{\odot}$; compare the top-left panels of Figs 13 and 14) together with the fact that emission lines are more robustly derived in low-S/N spectra than absorption lines.

4 DISCUSSION

We derive host galaxy stellar population parameters for SNe Ia from the SDSS-II Supernova Survey. These parameters are derived from absorption line indices through comparison with stellar population model predictions (see Section 2.2). Due to the low S/N of the host galaxy spectra, we focus on the highest quality objects, considering both the SN Ia observations and host galaxies, which results in a final sample of 84 objects (see Section 2.3).

We find a strong relationship between the SALT2 stretch factor and stellar population age (see Section 3.3). For SALT2 colour on the other hand, we do not find dependences on any of the host galaxy parameters, in agreement with previous studies. We also derive photometric stellar masses for the host galaxies using a variety of methods and models. The HR–stellar mass relation is found to behave as a sloped step function, where the trend is flat at the high-mass end (see Section 3.4.2). This is also the mass regime covered by our host spectroscopy sample, which may explain a lack of trends between HR and the stellar population parameters studied.

4.1 Progenitor systems

Considering several different progenitor systems, theoretical models of SN Ia explosions predict SN Ia delay-time distributions (DTDs) peaking below or close to 1 Gyr (Yungelson & Livio 2000; Greggio 2005; Ruiter et al. 2011). The SNRs then decline and become ∼100 times lower at delay times of ∼10 Gyr. Thus, theory implies that the delay times of SNe Ia span the range from relatively quick events to explosions delayed by a Hubble time.

Using the host galaxy stellar population ages as delay-time proxies, observed DTDs support theoretical models of declining SNRs following an $\sim t^{-1}$ power law (Maoz et al. 2012). Further support for a wide range of delay times is found in this work where we present SN Ia host galaxies with luminosity-weighted ages from below 1 Gyr to >10 Gyr. Similarly, Gupta et al. (2011) find SN Ia events in stellar populations with mass-weighted ages >10 Gyr and down to ∼2 Gyr, while Howell et al. (2009) and Neill et al. (2009) present luminosity-weighted ages from ∼100 Myr up to >10 Gyr. The work of Brandt et al. (2010) suggests delay times of <400 Myr and >2.4 Gyr, indicative of two different progenitor channels. Hence, the different stellar ages of SN Ia host galaxies reported by these studies confirm the conclusion of Förster et al. (2006) that the time-delay estimate is dominated by systematic errors due to uncertainties in the derived star formation history. All the studies mentioned above agree with theory such that a higher fraction of SN Ia events are found in young star-forming galaxies compared to old passively evolving galaxies.

We find a strong anticorrelation between the stretch factor and stellar population age (see Section 3.3). Since stellar lifetimes are strongly mass dependent, there is a connection such that those SNe Ia with the most massive WD progenitors, i.e. shortest delay times, are the most luminous (highest stretch factors) and vice versa. Contrary to Brandt et al. (2010), the relation between the stretch factor and stellar population age found in this work tentatively shows a smooth behaviour which may be indicative of a single SN Ia progenitor system. If SN Ia peak luminosity increases with WD-progenitor mass, the wider range of stellar masses in star-forming galaxies together with short lifetimes for massive stars result in the higher SN Ia fractions.

Yungelson & Livio (2000) show that the SNR for a DD system peaks at delay times of ∼100 Myr, while the analogous for an SD system is ∼1 Gyr. Thus, the lower age limit of the stellar populations hosting SNe Ia could be used to constrain possible progenitor systems. However, it may be unreasonable to attribute the integrated light of a galaxy to be a good proxy for SN Ia delay times, considering the range of stellar populations, age and metallicity, possibly present within an instrumental aperture. An alternative approach could be to use observations confined to the vicinity of the SNe Ia. However, it is likely that a mixing of stellar populations occurs over a long time span. The probability of identifying the 'true' parent stellar population for an SN Ia progenitor should increase for younger stellar populations. It may therefore be possible to constrain the lower delay-time limit using the stellar populations in the vicinity of the SNe Ia. This information can then in turn constrain possible progenitor systems when comparing to theoretical SN Ia models.

4.2 HR minimization

The reports of HR dependences on host galaxy mass (Kelly et al. 2010; Sullivan et al. 2010; Conley et al. 2011; Gupta et al. 2011) have led to the inclusion of this parameter to further reduce the scatter in the redshift–distance relation (e.g. L10; Sullivan et al. 2010). In this work, we find systematic uncertainties in the derived masses, due to the adopted SED-fitting prescription, to affect the HR–mass relationship (see Section 3.4.1). However, these systematic uncertainties become weaker when the number of galaxies is increased (see Section 3.4.2).

We also find that the stellar mass range covered affects the derived HR–mass trend (see Section 3.4.2). This trend behaves as a sloped step function, where the low- and, in particular, the high-mass ends show flat trends. Due to this sloped step function, the stellar mass range sampled will result in a systematic variation of the derived HR–mass slope. Hence, the sloped step function of the HR–mass relationship should be accounted for when using stellar mass as a further parameter for minimizing the HR. Constant step functions have been used in the literature for minimizing the HR (Sullivan et al. 2010, 2011; Conley et al. 2011).

The dependence of HR on stellar mass is believed to be a consequence of a dependence on a more fundamental parameter. The sampling of the high-mass regime of our host spectroscopy sample, where the trend between HR and stellar mass is flat, hampers a conclusion on which parameter is driving HR variations.

Interestingly, the step in the HR–mass plane appears at around $\sim 2 \times 10^{10}$ $M_{\odot}$ which is close to the evolutionary transition mass of low-redshift galaxies, discovered by Kauffmann et al. (2003a). They find that below $\sim 3 \times 10^{10}$ $M_{\odot}$, galaxies are typically disc-like objects with young stellar populations and low surface mass densities. Above this limit, they instead find an increasing fraction of bulge-dominated galaxies with old stellar populations. Hence, the transition mass marks a change in the stellar populations of galaxies. The similar mass range shared between the sudden shift in the HR and transition in galaxy properties is therefore most likely not coincidental. The stellar populations below and above the transition mass bare witness of the properties of the SN Ia progenitors with high and low HR, respectively. If the HR–mass relation is indeed flat at the low-mass end (only tentative due to low number statistics) as it is at the high-mass end, it may indicate two samples of SNe Ia with high and low HR, i.e. showing a weak difference in peak luminosity not accounted for by the LC fitting techniques.

The overlap in mass for the galaxy evolutionary transition and change in HR tells us that the latter does not change significantly in old, passively evolving stellar populations. Instead, there is a strong variation in lower mass galaxies with younger stellar populations, higher SFRs and lower gas-phase metallicities (Tremonti et al. 2004). Indeed, several authors suggest gas-phase metallicity to be the fundamental parameter driving HR variations (Howell et al. 2009; Sullivan et al. 2010; D'Andrea et al. 2011; Hayden et al. 2013). Also in this work we find tentative results for such a relation between HR and gas-phase metallicity (see Section 3.4.1). If this is indeed the fundamental parameter, it represents progenitor metallicity. This is in agreement with theoretical predictions of prompt SNe Ia in star-forming galaxies (Yungelson & Livio 2000; Greggio 2005; Ruiter et al. 2011). The flat slope at masses above $\sim 2 \times 10^{10}$ $M_{\odot}$ is then expected as the gas-phase metallicities show a flat behaviour in this mass regime (Tremonti et al. 2004; Hayden et al. 2013). However, prompt SNe Ia are not expected in old stellar populations present in passively evolving, massive galaxies. The derivation of the full range of stellar population parameters and gas-phase properties for a high-quality data set, covering the full mass range, is required to determine the fundamental parameter driving HR variations.

Future data from integral field unit spectroscopy, sampling the local environment of SNe Ia will be quite useful in identifying the fundamental parameter responsible for the scatter in the HR. For such data sets, it will be important to sample the full stellar mass range, in particular the mass range around 10^{10} $M_{\odot}$.

5 CONCLUSIONS

We present an analysis of the stellar populations of SN Ia host galaxies using SDSS-II spectroscopy. Using the stellar population models of absorption line indices from TMJ, we derive the stellar population parameters age, metallicity and element abundance ratios to study relationships with SN Ia properties. We also measure stellar velocity dispersion from stellar template fitting and gas-phase metallicity from emission lines when detected. Furthermore, we derive stellar masses and revisit the correlation between HR and stellar mass that has recently received much attention in the literature. The stellar masses are derived from SDSS-II photometry from repeat Stripe 82 observations and several SED-fitting methods. From a sample of 292 SNe Ia, we select 84 objects depending on the quality of the host galaxy spectroscopy and accuracy of the SN Ia properties (see Section 2.3).

We find a larger fraction of SNe Ia together with typically higher SALT2 stretch factor values (i.e. more luminous SNe Ia with slower declining LC) in star-forming compared to passively evolving galaxies (see Section 3.3), in agreement with the literature. Hence, previous studies suggest that the decline rate and peak luminosity of SNe Ia depend on stellar population age. With the large parameter space covered in this work, we indeed find that SALT2 stretch factor values show a strong dependence on stellar population age in the sense of a clear anticorrelation (see Section 3.3). As a result of this trend, we also find anticorrelations with velocity dispersion and galaxy mass, while only weak anticorrelations are also found for stellar metallicity and the element abundance ratios studied.

To ensure that the quality of the host galaxies is not affecting the selected sample, we stacked the spectra in bins of stretch factor. This exercise confirms the above results that stellar age is a strong candidate for the main driver of SN Ia luminosity (see Section 3.3.2). Hence, SN Ia peak luminosity is closely related to the age of the stellar progenitor systems, where more luminous SNe Ia appear in young stellar populations.

The peak-luminosity variation of SNe Ia is corrected for through LC fitting. However, scatter in the redshift–distance relation even after these corrections may introduce uncertainties in derived cosmological parameters. It has been debated which parameter could be used to further minimize this scatter. While stellar mass has already been introduced for this purpose, stellar population age and metallicity as well as gas-phase metallicity have been proposed as fundamental parameters for the HR dependence.

However, we identify no statistically significant trends of HR with any of the stellar population parameters studied or with stellar velocity dispersion (see Section 3.4.1). Instead, we find tentative results confirming a trend between HR and gas-phase metallicity as previously reported. For the HR–stellar mass relationship, our selected sample shows a weak trend that is affected by the method of stellar mass derivation. Stellar masses that show the tightest correlation with stellar velocity dispersion produce the weakest trend with HR. To study this in more detail, we extend the sample to include 102 SNe Ia with available SDSS host galaxy photometry

and lift the spectroscopic quality constraints, resulting in a sample of 247 objects for deriving stellar masses from SDSS photometry. With the better statistics of this larger sample, the systematic variations arising from the stellar mass derivation are weakened (see Section 3.4.2).

For the extended photometric sample, it is clear that the reported HR–mass relation is strongly dependent on the stellar mass range studied and behaves as a sloped step function. In the high-mass regime, the relation between HR and stellar mass is flat. Since our sample with available host galaxy spectroscopy mainly probes this high-mass regime, it is not surprising that we do not find any significant HR trend with the stellar population parameters studied. Below a stellar mass of $\sim 2 \times 10^{10}\,M_{\odot}$, i.e. close to the evolutionary transition mass of low-redshift galaxies reported in the literature, the trend changes dramatically such that lower mass galaxies exhibit fainter SNe Ia after LC corrections. We conclude that the sloped step function of the HR–mass relationship should be accounted for if stellar mass is to be used as a further parameter for minimizing the HR. Constant step functions have been used in the literature for minimizing the HR (Sullivan et al. 2010, 2011; Conley et al. 2011). However, it is crucial to find the fundamental parameter driving systematic variations in the HR.

ACKNOWLEDGEMENTS

We thank Rita Tojeiro for helpful discussions and an anonymous referee for useful comments that helped improve this paper.

Funding for the SDSS and SDSS-II has been provided by the Alfred P. Sloan Foundation, the Participating Institutions, the National Science Foundation, the US Department of Energy, the National Aeronautics and Space Administration, the Japanese Monbukagakusho, the Max Planck Society and the Higher Education Funding Council for England. The SDSS website is http://www.sdss.org/.

The SDSS is managed by the Astrophysical Research Consortium for the Participating Institutions. The Participating Institutions are the American Museum of Natural History, Astrophysical Institute Potsdam, University of Basel, University of Cambridge, Case Western Reserve University, University of Chicago, Drexel University, Fermilab, the Institute for Advanced Study, the Japan Participation Group, Johns Hopkins University, the Joint Institute for Nuclear Astrophysics, the Kavli Institute for Particle Astrophysics and Cosmology, the Korean Scientist Group, the Chinese Academy of Sciences (LAMOST), Los Alamos National Laboratory, the Max-Planck-Institute for Astronomy (MPIA), the Max-Planck-Institute for Astrophysics (MPA), New Mexico State University, Ohio State University, University of Pittsburgh, University of Portsmouth, Princeton University, the United States Naval Observatory and the University of Washington.

REFERENCES

Abazajian K. et al., 2009, ApJS, 182, 543
Annis J. et al., 2011, preprint (arXiv:1111.6619)
Arnett W., 1982, ApJ, 253, 785
Aubourg É., Tojeiro R., Jimenez R., Heavens A., Strauss M., Spergel D., 2008, A&A, 492, 631
Baldwin J., Phillips M., Terlevich R., 1981, PASP, 93, 5 (BPT)
Barris B., Tonry J., 2006, ApJ, 637, 427
Beifiori A., Maraston C., Thomas D., Johansson J., 2011, A&A, 531, 109
Bolzonella M., Miralles J.-M., Pelló R., 2000, A&A, 363, 476
Branch D., 2001, PASP, 113, 169
Branch D., Livio M., Yungelson L., Boffi F., Baron E., 1995, PASP, 107, 1019
Brandt T., Tojeiro R., Aubourg É., Heavens A., Jimenez R., Strauss M., 2010, AJ, 140, 804
Bruzual G., Charlot S., 2003, MNRAS, 344, 1000 (BC03)
Campbell H. et al., 2013, ApJ, 763, 88
Cappellari M., Emsellem E., 2004, PASP, 116, 138
Childress M. et al., 2013, ApJ, 770, 108
Colgate S., McKee C., 1969, ApJ, 157, 623
Conley A. et al., 2008, ApJ, 681, 482
Conley A. et al., 2011, ApJS, 192, 1
Cooper M. C., Newman J. A., Yan R., 2009, ApJ, 704, 687
D'Andrea C. et al., 2011, ApJ, 743, 172
Daddi E. et al., 2005, ApJ, 626, 680
Dilday B. et al., 2010, ApJ, 713, 1026
Ferraro F. R., Origlia L., Testa V., Maraston C., 2004, ApJ, 608, 772
Fioc M., Rocca-Volmerange B., 1997, A&A, 326, 950
Fioc M., Rocca-Volmerange B., 1999, preprint (astro-ph/9912179)
Förster F., Wolf C., Podsiadlowski Ph., Han Z., 2006, MNRAS, 368, 1893
Frieman J. et al., 2008, AJ, 135, 338
Fukugita M., Ichikawa T., Gunn J. E., Doi M., Shimasaku K., Schneider D. P., 1996, AJ, 111, 1748
Gal-Yam A., Maoz D., 2004, MNRAS, 347, 942
Gallagher J. S., Garnavich P. M., Berlind P., Challis P., Jha S., Kirshner R., 2005, ApJ, 634, 210
Gallagher J., Garnavich P., Caldwell N., Kirshner R., Jha S., Li W., Ganeshalingam M., Filippenko A., 2008, ApJ, 685, 752
Gallazzi A., Charlot S., Brinchmann J., White S., Tremonti C., 2005, MNRAS, 362, 41
Greggio L., 2005, A&A, 441, 1055
Gunn J. E. et al., 1998, AJ, 116, 3040
Gunn J. E. et al., 2006, AJ, 131, 2332
Gupta R. et al., 2011, ApJ, 740, 92
Guy J. et al., 2007, A&A, 466, 11
Hamuy M., Trager S., Pinto P., Phillips M., Schommer R., Ivanov V., Suntzeff N., 2000, AJ, 120, 1479
Hansson A., Lisker T., Grebel E., 2012, MNRAS, 427, 2376
Hayden B. T., Gupta R. R., Garnavich P. M., Mannucci F., Nichol R. C., Sako M., 2013, ApJ, 764, 191
Hillebrandt W., Niemeyer J., 2000, ARA&A, 38, 191
Hoflich P., Khokhlov A., Wheeler J., 1995, ApJ, 444, 831
Holtzman J. A. et al.2008, AJ, 136, 2306
Howell D. et al., 2009, ApJ, 691, 661
Jha S., Riess A., Kirshner R., 2007, ApJ, 659, 122
Johansson J., Thomas D., Maraston C., 2010, MNRAS, 406, 165
Johansson J., Thomas D., Maraston C., 2012, MNRAS, 421, 1908
Kasen D., Röpke F., Woosley S., 2009, Nat, 460, 869
Kauffmann G. et al., 2003a, MNRAS, 341, 54
Kauffmann G. et al., 2003b, MNRAS, 346, 1055
Kelly P., Hicken M., Burke D., Mandel K., Kirshner R., 2010, ApJ, 715, 743
Kessler R. et al., 2009a, PASP, 121, 1028
Kessler R. et al., 2009b, ApJS, 185, 32
Kewley L., Dopita M., 2002, ApJS, 142, 35 (KD02)
Kewley L., Ellison S., 2008, ApJ, 681, 1183
Kewley L., Dopita M., Sutherland R., Heisler C., Trevena J., 2001, ApJ, 556, 121
Korn A., Maraston C., Thomas D., 2005, A&A, 438, 685
Lampeitl H. et al., 2010a, MNRAS, 401, 2331
Lampeitl H. et al., 2010b, ApJ, 722, 566 (L10)
Lee J., Hwang H., Lee M., Lee J., Matsuhara H., 2010, ApJ, 719, 1946
MacArthur L., 2005, ApJ, 623, 795
Mannucci F., Della Valle M., Panagia N., Cappellaro E., Cresci G., Maiolino R., Petrosian A., Turatto M., 2005, A&A, 433, 807
Mannucci F., Cresci G., Maiolino R., Marconi A., Gnerucci A., 2010, MNRAS, 408, 2115
Maoz D., Mannucci F., Brandt T. D., 2012, MNRAS, 426, 3282
Maraston C., 2005, MNRAS, 362, 799 (M05)
Maraston C., Strömbäck G., 2011, MNRAS, 418, 2785
Maraston C., Daddi E., Renzini A., Cimatti A., Dickinson M., Papovich C., Pasquali A., Pirzkal N., 2006, ApJ, 652, 85

Maraston C., Pforr J., Renzini A., Daddi E., Dickinson M., Cimatti A., Tonini C., 2010, MNRAS, 407, 830
Neill J. et al., 2009, ApJ, 707, 1449
Oemler A., Jr, Tinsley B., 1979, AJ, 84, 985
Perlmutter S. et al., 1999, ApJ, 517, 565
Pettini M., Pagel B., 2004, MNRAS, 348, 59 (PP04)
Pforr J., Maraston C., Tonini C., 2012, MNRAS, 422, 3285
Phillips M., 1993, ApJ, 413, 105
Podsiadlowski P., Mazzali P., Lesaffre P., Han Z., Förster F., 2008, New Astron. Rev., 52, 381
Renzini A., 2006, ARA&A, 44, 141
Riess A. G. et al., 1998, AJ, 116, 1009
Riess A. G. et al., 2011, ApJ, 730, 119
Ruiter A., Belczynski K., Sim S., Hillebrandt W., Fryer C., Fink M., Kromer M., 2011, MNRAS, 417, 408
Sako M. et al., 2008, AJ, 135, 348
Sánchez-Blázquez P. et al., 2006, MNRAS, 371, 703
Sarzi M. et al., 2006, MNRAS, 366, 1151
Schawinski K., Thomas D., Sarzi M., Maraston C., Kaviraj S., Joo S.-J., Yi S. K., Silk J., 2007, MNRAS, 382, 1415
Serra P., Trager S., 2007, MNRAS, 374, 769
Smee S. A. et al., 2012, AJ, 146, 32
Smith M. et al., 2012, ApJ, 755, 61
Sollerman J. et al., 2009, ApJ, 703, 1374
Strauss M. et al., 2002, AJ, 124, 1810
Strolger L.-G. et al., 2004, ApJ, 613, 200
Strolger L.-G. et al., 2005, ApJ, 635, 1370
Sullivan M. et al., 2006, ApJ, 648, 868
Sullivan M. et al., 2010, MNRAS, 406, 782
Sullivan M. et al., 2011, ApJ, 737, 102
Thomas D., Maraston C., Bender R., 2003, MNRAS, 339, 897
Thomas D., Maraston C., Schawinski K., Sarzi M., Silk J., 2010, MNRAS, 404, 1775
Thomas D., Maraston C., Johansson J., 2011, MNRAS, 412, 2183 (TMJ)
Timmes F., Brown E., Truran J., 2003, ApJ, 590, 83
Trager S. C., Worthey G., Faber S. M., Burstein D., Gonzalez J. J., 1998, ApJS, 116, 1
Tremonti C. A. et al., 2004, ApJ, 613, 898
Umeda H., Nomoto K., Kobayashi C., Hachisu I., Kato M., 1999, ApJ, 522, 43
van den Bergh S., 1990, PASP, 102, 1318
Whelan J., Iben I., Jr, 1973, ApJ, 186, 1007
Woosley S., Weaver T., 1986, ARA&A, 24, 205
Worthey G, Faber S. M., Gonzalez J. J., Burstein D., 1994, ApJS, 94, 687
Worthey G., Ottaviani D. L., 1997, ApJS, 111, 377
York D. et al., 2000, AJ, 120, 1579
Yungelson L., Livio M., 2000, ApJ, 528, 108

SUPPORTING INFORMATION

Additional Supporting Information may be found in the online version of this article:

Appendix A: Specifications for the host spectroscopy sample (http://mnras.oxfordjournals.org/lookup/suppl/doi:10.1093/mnras/stt1408/-/DC1).

Please note: Oxford University Press are not responsible for the content or functionality of any supporting materials supplied by the authors. Any queries (other than missing material) should be directed to the corresponding author for the article.

This paper has been typeset from a TEX/LATEX file prepared by the author.